

GAMMA-RAY BURST DYNAMICS AND AFTERGLOW RADIATION FROM ADAPTIVE MESH REFINEMENT, SPECIAL RELATIVISTIC HYDRODYNAMIC SIMULATIONS

FABIO DE COLLE¹, JONATHAN GRANOT^{2,3,4}, DIEGO LÓPEZ-CÁMARA⁵, AND ENRICO RAMIREZ-RUIZ¹

¹ Astronomy & Astrophysics Department, University of California, Santa Cruz, CA 95064, USA; fabio@ucolick.org

² Racah Institute of Physics, The Hebrew University, Jerusalem 91904, Israel

³ Raymond and Beverly Sackler School of Physics & Astronomy, Tel Aviv University, Tel Aviv 69978, Israel

⁴ Centre for Astrophysics Research, University of Hertfordshire, College Lane, Hatfield, AL10 9AB, UK

⁵ Instituto de Ciencias Nucleares, Universidad Nacional Autónoma de México, Ap. 70-543, 04510 D.F., Mexico

Received 2011 August 1; accepted 2011 November 22; published 2012 January 31

ABSTRACT

We report on the development of Mezcál-SRHD, a new adaptive mesh refinement, special relativistic hydrodynamics (SRHD) code, developed with the aim of studying the highly relativistic flows in gamma-ray burst sources. The SRHD equations are solved using finite-volume conservative solvers, with second-order interpolation in space and time. The correct implementation of the algorithms is verified by one-dimensional (1D) and multi-dimensional tests. The code is then applied to study the propagation of 1D spherical impulsive blast waves expanding in a stratified medium with $\rho \propto r^{-k}$, bridging between the relativistic and Newtonian phases (which are described by the Blandford–McKee and Sedov–Taylor self-similar solutions, respectively), as well as to a two-dimensional (2D) cylindrically symmetric impulsive jet propagating in a constant density medium. It is shown that the deceleration to nonrelativistic speeds in one dimension occurs on scales significantly larger than the Sedov length. This transition is further delayed with respect to the Sedov length as the degree of stratification of the ambient medium is increased. This result, together with the scaling of position, Lorentz factor, and the shock velocity as a function of time and shock radius, is explained here using a simple analytical model based on energy conservation. The method used for calculating the afterglow radiation by post-processing the results of the simulations is described in detail. The light curves computed using the results of 1D numerical simulations during the relativistic stage correctly reproduce those calculated assuming the self-similar Blandford–McKee solution for the evolution of the flow. The jet dynamics from our 2D simulations and the resulting afterglow light curves, including the jet break, are in good agreement with those presented in previous works. Finally, we show how the details of the dynamics critically depend on properly resolving the structure of the relativistic flow.

Key words: gamma-ray burst: general – hydrodynamics – methods: numerical – radiation mechanisms: non-thermal – relativistic processes – shock waves

Online-only material: color figures

1. INTRODUCTION

Gamma-ray bursts (GRBs) are the most electromagnetically luminous explosions in the universe. Their nonthermal and highly variable gamma-ray emission implies that the emitting region must be ultrarelativistic—moving with a very large Lorentz factor, typically $\gtrsim 100$ and sometimes as high as $\gtrsim 10^3$, in order to avoid excessive pair production at the source (e.g., Lithwick & Sari 2001; Granot et al. 2008; Abdo et al. 2009a, 2009b; Ackermann et al. 2010). At sufficiently large distances from the source the GRB outflow decelerates as it drives a strong relativistic shock into the surrounding medium (for reviews see, e.g., Piran 2005a; Granot 2007). Synchrotron emission from this long-lived external shock powers the GRB afterglow, which is observed in the X-rays, optical or radio, typically over days to months after the prompt gamma-ray emission. The peak frequency of the afterglow emission shifts to lower energies as the afterglow shock decelerates by sweeping up the external medium (Rees & Meszaros 1992). This picture of a decelerating relativistic expansion of the emitting region during the afterglow phase is supported by direct measurements of the afterglow image size at late times in the radio, using very long baseline interferometric techniques, for GRB 030329 at $z = 0.1685$ (Taylor et al. 2004, 2005; Pihlström et al. 2007).

GRB activity manifests itself over a dynamical range of ~ 13 decades in radius (Gehrels et al. 2009). The phenomena involve

different stages, which are usually modeled separately because of their complexity. Let us consider these stages in turn, working from the small scales to the large scales.

1.1. Jet Production and the Central Engine

GRBs are divided into two classes according to their duration and spectral hardness (Kouveliotou et al. 1993). Long-duration GRBs (lasting $\gtrsim 2$ s) are associated with Type Ic core-collapse supernovae and thus with the death of massive stars (Stanek et al. 2003; Hjorth et al. 2003; Woosley & Bloom 2006), while the nature of short-duration GRB (lasting $\lesssim 2$ s) progenitors is still debated (Lee & Ramirez-Ruiz 2007; Nakar 2007), the most popular model involving the binary merger of two compact stars (Paczynski 1986; Eichler et al. 1989; Narayan et al. 1992).

In the collapsar model for long GRBs (Woosley 1993), during the collapse of a massive Wolf-Rayet progenitor star a black hole is formed, which rapidly accretes stellar envelope material, launching a relativistic jet that penetrates the star and eventually powers the GRB (Ramirez-Ruiz et al. 2002). It has been modeled using numerical simulations, where a jet is usually injected as an inner boundary condition at the center of a collapsing massive star and bores its way out of the progenitor star's envelope (MacFadyen & Woosley 1999; Zhang et al. 2003). Some simulations include a magnetic field (in an ideal magnetohydrodynamical framework) and recently added a general relativistic framework (Mizuno et al. 2004a, 2004b;

Hawley & Krolik 2006; McKinney 2006; Nagataki et al. 2007; Tchekhovskoy et al. 2008; Nagataki 2009; Barkov & Baushev 2011). The alternative model for the central engine of long GRBs featuring the formation of a millisecond magnetar (i.e., a very rapidly rotating highly magnetized neutron star; Usov 1992) has also been studied numerically (Komissarov & Barkov 2007; Bucciantini et al. 2007, 2008, 2009). Binary merger simulations of two neutron stars or a neutron star and a black hole were performed in the context of short GRBs (Lee & Ramirez-Ruiz 2002; Rosswog & Ramirez-Ruiz 2002; Rosswog 2005; Faber et al. 2006; Oechslin & Janka 2006; Rezzolla et al. 2010). Recent general relativistic magnetohydrodynamic (MHD) simulations show that a relativistic jet can naturally form in such a scenario, which may indeed power short GRBs (Rezzolla et al. 2011). Similar simulations of relativistic jet formation from accretion onto a black hole are routinely performed also in the context of active galactic nuclei or microquasars (e.g., Meier 2003; Krolik & Hawley 2010). Different processes have been suggested to accelerate and collimate the jet: (1) thermal energy injected into the jet by annihilation of neutrinos and anti-neutrinos from an accretion disk (e.g., Fryer & Woosley 1998; Popham et al. 1999; Rosswog et al. 2003; Lee et al. 2004; Lee & Ramirez-Ruiz 2006; Chen & Beloborodov 2007); (2) rotational energy extracted from the central black hole through the Blandford–Znajek effect (Blandford & Znajek 1977; Meszaros & Rees 1997; Barkov & Komissarov 2008); and (3) rotational energy extracted from the accretion disk, coupled with a dynamically important magnetic field (Blandford & Payne 1982; Proga et al. 2003; Lynden-Bell 2003; Uzdensky & MacFadyen 2006).

1.2. Jet Expansion and Deceleration

Once the GRB outflow transfers most of its energy to the shocked external medium, it becomes dynamically subdominant and the flow becomes insensitive to the exact composition or initial radial structure of the original outflow. At this stage a spherical flow approaches the Blandford & McKee (1976, hereafter BMK) self-similar solution, losing memory of the initial conditions and retaining memory only of the total energy. The complete evolution of a spherical relativistic fireball, including the acceleration, coasting, and deceleration phases, has been studied numerically by Kobayashi et al. (1999) by using one-dimensional (1D) spherical simulations.

When a nonspherical relativistic outflow (or jet) decelerates, to zeroth order it locally resembles a section of the spherical BMK solution characterized by the local value of the energy per solid angle or isotropic equivalent kinetic energy, $E_{k, \text{iso}}$. Once the Lorentz factor Γ drops to θ_0^{-1} , where θ_0 is the initial half-opening angle of an initially uniform jet with sharp edges, the jet becomes causally connected in the lateral direction and can in principle start spreading sideways significantly. Simple analytic models argue that it should indeed quickly spread sideways (Rhoads 1997, 1999; Sari et al. 1999), while numerical simulations show that the lateral spreading is much more modest, and the flow retains memory of θ_0 for a long time, which for typical values of θ_0 in GRBs lasts up to the nonrelativistic transition time (Granot et al. 2001; Granot & Königl 2003; Cannizzo et al. 2004; Zhang & MacFadyen 2009).

The numerical simulations of jet dynamics during the afterglow stage are usually done separately from the earlier stages (of the jet formation, acceleration, and collimation), in order to simplify these challenging numerical computations, which involve a very large dynamical range. The most common initial

conditions for simulations of the GRB jet during the afterglow stage are a conical wedge of half-opening angle θ_0 taken out of the spherical BMK solution (though in some cases a relativistic cold shell or blob is used instead). Since the angular size of regions that are casually connected in the lateral direction is $\sim 1/\Gamma$, such a BMK wedge should not evolve significantly while its Lorentz factor is $\Gamma \gg \theta_0^{-1}$, suggesting that the subsequent evolution should be insensitive to the exact choice of initial Lorentz factor Γ_0 in the limit where $\Gamma_0 \gg \theta_0^{-1}$.

For an ultrarelativistic blast wave most of the energy in the shocked (downstream) region is within a thin layer behind the shock transition, whose width is $\Delta \sim 0.1R/\Gamma^2$ in the lab frame (i.e., the rest frame of the external or upstream medium, which in our case is also that of the central source), which is hard to resolve properly for large initial Lorentz factors (see, e.g., Granot 2007). Therefore, most simulations use $\Gamma_0\theta_0 \sim 3\text{--}4$ rather than the ideal choice of $\Gamma_0\theta_0 \gg 1$, along with values of θ_0 that are not very small (usually $\theta_0 = 0.2$ and $\Gamma_0 \sim 20$), despite the fact that the actual initial Lorentz factors at the onset of the afterglow are estimated to be at least a few hundred (e.g., Lithwick & Sari 2001), while the values of θ_0 inferred from afterglow observations (e.g., Frail et al. 2001) can be as low as $\sim 0.03\text{--}0.05$ (or as high as $\gtrsim 0.5$).

1.3. Afterglow Jet Simulations: Previous Work and Goals

Since afterglow emission is thought to be predominantly synchrotron radiation from the shocked external medium, then accurately inferring the properties of the original relativistic outflow and the external medium from afterglow observations requires an accurate modeling of the dynamics. The jet numerical simulations and calculations of the corresponding afterglow emission (Granot et al. 2001) have recently been extended to well within the nonrelativistic stage (e.g., Zhang & MacFadyen 2009; van Eerten et al. 2010; Wygoda et al. 2011; van Eerten & MacFadyen 2011). Following the dynamics from a highly ultrarelativistic initial Lorentz factor ($\Gamma_0 > 20$, for which $\Delta_0/R_0 \sim 10^{-4}(\Gamma_0/30)^{-2}$) down to highly Newtonian velocities ($v < 0.01c$) requires a very large range of spatial scales, for which an adaptive mesh refinement (AMR) code is necessary in order to properly calculate the multi-dimensional flow dynamics. Granot et al. (2001) were the first to study this problem numerically by using multi-dimension numerical simulations and found that the GRB jet sideways expansion is slower than expected from analytical models. These results were later confirmed by Zhang & MacFadyen (2009), who followed the evolution of the GRB jet up to the nonrelativistic phase by running high-resolution two-dimensional (2D) simulations. Simulations using similar initial conditions were also run by Meliani & Keppens (2010), who found that the shock front becomes unstable at high values of the Lorentz factor, $\Gamma \gtrsim 15$, but the instabilities quickly decay when the jet decelerates to $\Gamma \lesssim 10$.

All the multi-dimensional numerical simulations of afterglow jets have so far assumed a uniform external medium, even though a stratified external medium is expected for the stellar wind of a massive star long GRB progenitor (Chevalier & Li 2000; Panaitescu & Kumar 2000; Ramirez-Ruiz et al. 2001, 2005). This was partly motivated by the faster deceleration of the afterglow shock with radius in a uniform external medium compared with a stratified one, which reduces the required dynamical range of the simulations. Moreover, magnetic fields may also affect the jet dynamics (in addition to their effect on the afterglow synchrotron radiation). Mimica et al. (2009, 2010) have used 1D simulations to study the deceleration of

magnetized GRB ejecta propagating into a uniform ambient medium and showed that while the late evolution of strongly magnetized shells resembles that of hydrodynamic shells, the magnetization plays an important role in the onset of the forward shock emission. Mimica & Giannios (2011) computed the afterglow emission produced by a GRB ejecta decelerating into a realistic external medium by running 1D spherical simulations. However, multi-dimensional simulations are necessary in order to fully capture the magnetic field dynamics, such as the generation of turbulence by the MHD Kelvin-Helmholtz (Zhang et al. 2009) or Richtmyer–Meshkov (Goodman & MacFadyen 2008) instabilities and the consequent magnetic field amplification (Inoue et al. 2011; Mizuno et al. 2011). Actually, Granot et al. (2011) have recently shown that even in 1D one cannot realistically model the deceleration stage separately from the acceleration stage if the outflow is initially highly magnetized and accelerates under its own magnetic pressure. Instead, a full simulation of the acceleration and deceleration is needed, requiring a very large dynamical range that is numerically challenging.

With the aim of addressing these questions and perhaps also possible applicability to earlier stages of the jet dynamics (such as its acceleration or propagation within the progenitor star), we have developed a new AMR, relativistic hydrodynamic code. While the code developed is similar in several aspects to previous SRHD-AMR codes (e.g., Hughes et al. 2002; Anninos et al. 2005; Zhang & MacFadyen 2009; Meliani et al. 2007; Morsony et al. 2007; Wang et al. 2008), we consider it important to present a detailed, self-contained description of the hydrodynamic code and the matching radiation code, along with detailed tests. The paper is organized as follows. Sections 2 and 3 describe in detail, respectively, the special relativistic hydrodynamics (SRHD) code and the radiation code used to calculate the observed afterglow emission (by post-processing the outcome of the SRHD simulation). Standard tests used to verify the SRHD code are presented in Appendix B, while the correct implementation of the radiation code is discussed in Section 4. Section 4 presents a detailed study of the propagation of a relativistic, purely hydrodynamic ejecta into a 1D stratified medium and in a multi-dimensional homogeneous medium together with the resulting light curves. Finally, Section 5 presents our conclusions. Simulations of the propagation of jets into a stratified medium and the inclusion of magnetized flows will be addressed in future work.

2. NUMERICAL CODE

2.1. Relativistic Hydrodynamic Equations

The SRHD equations in conservative form (e.g., Anile 1989) can be written as follows:

$$\frac{\partial D}{\partial t} + \nabla \cdot (D\vec{v}) = 0 \quad (1)$$

$$\frac{\partial \vec{S}}{\partial t} + \nabla \cdot (\vec{S}\vec{v} + p\mathcal{I}) = 0 \quad (2)$$

$$\frac{\partial \tau}{\partial t} + \nabla \cdot (\tau\vec{v} + p\vec{v}) = 0, \quad (3)$$

where p is the thermal pressure, $\vec{v} = \vec{\beta}c$ is the flow velocity (c being the speed of light), and \mathcal{I} is the identity matrix. These equations represent the conservation of rest mass (1),

momentum (2), and energy (3). The conserved variables (D, \vec{S}, τ) correspond to the lab frame rest mass, momentum, and energy (excluding rest mass) densities, respectively. They are related to the primitive variables (ρ, \vec{v}, p) by the following relations:

$$D = \rho\Gamma, \quad (4)$$

$$\vec{S} = Dh\Gamma\vec{v}, \quad (5)$$

$$\tau = Dh\Gamma c^2 - p - Dc^2, \quad (6)$$

where $\Gamma = (1 - \beta^2)^{-1/2}$ is the Lorentz factor, ρ is the proper rest-mass density, and h is the specific enthalpy. The SRHD system of equations is closed by the equation of state (EOS), relating h to p and ρ . Note that by explicitly subtracting the rest mass in the definition of the lab frame energy density τ in Equation (6), the nonrelativistic hydrodynamic equations are properly recovered when $\beta \ll 1$.

2.2. Integration Methods

The SRHD Equations (1)–(3) form a hyperbolic system of equations and can be solved by using methods similar to those developed for classical nonrelativistic gas dynamics (for a review see, e.g., Toro 2008). Without loss of generality, the solution of the hyperbolic system of equations

$$\frac{\partial u}{\partial t} + \nabla \cdot \vec{f} = 0 \quad (7)$$

is given in 1D (the generalization to multi-dimensions is straightforward) by

$$U_i^{n+1} = U_i^n - \frac{\Delta t}{\Delta x_i} (F_{i+1/2}^{n+1/2} - F_{i-1/2}^{n+1/2}), \quad (8)$$

where x_i represents the position of the center of the cell i with volume $\Delta x_i = x_{i+1/2} - x_{i-1/2}$, $x_{i\pm 1/2}$ are the positions of the interfaces between the cells x_i and $x_{i\pm 1}$, and

$$U_i^n = \frac{1}{\Delta x_i} \int_{x_{i-1/2}}^{x_{i+1/2}} u_i(t^n, x) dx \quad (9)$$

$$F_{i\pm 1/2}^{n+1/2} = \frac{1}{\Delta t} \int_{t_n}^{t_{n+1}} f(t, x_{i\pm 1/2}) dt \quad (10)$$

are the volume average of the conservative variables and their time-averaged fluxes.

While Equation (8) represents an exact solution of the corresponding partial differential equation, an approximation is introduced when the fluxes (Equation (10)) are computed. Because an exact solver is in general very expensive, in the current version of the code we have implemented the simple and computationally efficient relativistic extension (Schneider et al. 1993) of the Harten, Lax, and van Leer (HLL) method (Harten et al. 1983).

It is well known that the HLL method does not resolve properly the contact discontinuity, and it has an intrinsic high level of numerical diffusivity, while other methods (e.g., the HLL-Contact-Discontinuity or HLLC method; Mignone & Bodo 2005) properly reconstruct the contact discontinuity, producing results with significantly lower dissipation. On the

other hand, being more diffusive, the HLL method is also more “robust,” very rarely producing unphysical results such as negative pressures or imaginary Lorentz factors. In addition, a low dissipation method may produce undesirable effects, such as a “carbuncle” artifact along the axis of propagation of strong shocks (see the discussion by Wang et al. 2008).

Second-order accuracy in time and space is obtained by employing a Runge–Kutta integrator and by a spatial reconstruction of the primitive variables (van Leer 1979), except in shocks where the methods drop to first order (in space) by a limiter. Different limiters are implemented, including the “minmod” (being the most diffusive), UMIST, Superbee, and the less diffusive “monotonized central difference” limiter.

2.3. Extension to Cylindrical and Spherical Coordinates

The extension to cylindrical and spherical coordinates is treated very carefully in the code. For instance, in 2D (r, θ) spherical coordinates, the equations read

$$\frac{\partial U}{\partial t} + \frac{1}{r^2} \frac{\partial(r^2 F)}{\partial r} + \frac{1}{r \sin \theta} \frac{\partial(G \sin \theta)}{\partial \theta} = \frac{S}{r}, \quad (11)$$

where U , F , G , and S can be easily derived from Equations (1)–(3). We note that a simple cell-center discretization of this system of equations introduces large numerical errors when differencing. In particular, it does not preserve stationary initial conditions to machine accuracy. As an example, if one assumes static initial conditions, such as $\partial p / \partial r = 0$, ρ constant, and $\vec{v} = 0$, these are preserved in the code if, e.g., the relation (easily derived from the θ -component of the momentum equation)

$$\frac{1}{r \sin \theta} \frac{\partial(p \sin \theta)}{\partial \theta} = \frac{p \cos \theta}{r \sin \theta} \quad (12)$$

is held to machine accuracy. A simple centered discretization gives

$$\frac{1}{\sin \theta_j} \frac{\sin \theta_{j+1/2} - \sin \theta_{j-1/2}}{\theta_{j+1/2} - \theta_{j-1/2}} \neq \frac{\cos \theta_j}{\sin \theta_j}, \quad (13)$$

where θ_j is evaluated at the center of the cell, while $\theta_{j\pm 1/2}$ is evaluated at the interface between different cells, and it does not preserve the initial conditions.

A way to minimize numerical errors when differencing Equation (11), especially near coordinate singularities, is by a finite-volume discretization (e.g., Falle 1991; Li & Li 2003), that is, by averaging the variables over the cell volume. Given, for instance, the cell centered in (i, j) and with nodes located at $(i \pm 1/2, j \pm 1/2)$, the value of the quantity A averaged over the cell volume is given by

$$\langle A \rangle = \frac{\int \sin \theta d\theta \int A r^2 dr}{\int \sin \theta d\theta \int r^2 dr}. \quad (14)$$

With this definition, radial and polar derivatives are approximated by (taking $A = (1/r^2)((\partial(r^2 F))/\partial r)$ and $A = (1/(r \sin \theta))((\partial(G \sin \theta))/\partial \theta)$, respectively)

$$\begin{aligned} \frac{1}{r^2} \frac{\partial(r^2 F)}{\partial r} &\approx \frac{\delta_i(r^2 F)}{\delta_i(r^3/3)}, \\ \frac{1}{r \sin \theta} \frac{\partial(G \sin \theta)}{\partial \theta} &\approx \frac{\delta(G \sin \theta) \delta(r^2/2)}{-\delta(\cos \theta) \delta(r^3/3)}, \end{aligned} \quad (15)$$

where $\delta_i(f) = f_{i+1/2} - f_{i-1/2}$, while the source terms are discretized by assuming (taking $A = 1/r$ and $A = \cos \theta / \sin \theta$,

respectively)

$$\frac{1}{r} \approx \frac{\delta_i(r^2/2)}{\delta_i(r^3/3)}, \quad \frac{\cos \theta}{\sin \theta} \approx \frac{\delta(\sin \theta)}{-\delta(\cos \theta)}. \quad (16)$$

It is easy to verify that, written in this form, Equation (12) preserves static initial conditions to machine accuracy.

2.4. Equation of State

The EOS relates the enthalpy to the pressure and density. In the case of a relativistic perfect gas it takes the form (Synge 1971)

$$h = \frac{K_3(1/\Theta)}{K_2(1/\Theta)}, \quad (17)$$

where $\Theta = p/(\rho c^2)$ and K_i is the i th order of the modified Bessel functions of the second kind.

As the evaluation of the enthalpy from Equation (17) is computationally expensive (see, e.g., Falle & Komissarov 1996), simplified relations have been used, the simplest being the $\tilde{\gamma}$ -law EOS:

$$h = 1 + \frac{\tilde{\gamma}}{\tilde{\gamma} - 1} \Theta, \quad (18)$$

with a constant value of the adiabatic index $\tilde{\gamma}$ fixed and equal to 4/3 or 5/3, valid only in the limit of ultrarelativistic or subrelativistic fluids, respectively.

Mignone & Bodo (2005) proposed the EOS (see also Mathews 1971):

$$h = \frac{5}{2} \Theta + \frac{3}{2} \sqrt{\Theta^2 + \frac{4}{9}}, \quad (19)$$

which, in addition to approximating Equation (17) within 2%, also satisfies the Taub (1948) inequality

$$(h - \Theta)(h - 4\Theta) \leq 1 \quad (20)$$

in accordance with relativistic kinetic theory.

More recently, Ryu et al. (2006) proposed a simpler and better approximation to the Synge EOS (accurate to within 0.5%), which also satisfies the Taub inequality (Equation (20)), given by

$$h = 2 \frac{6\Theta^2 + 4\Theta + 1}{3\Theta + 2}. \quad (21)$$

The implementation of these EOS is straightforward, and unless stated otherwise, in this paper we use the one derived by Ryu et al. (2006).

2.5. Converting Conserved to Primitive Variables

The increased level of complexity in solving the SRHD equations when compared with the corresponding nonrelativistic hydrodynamic equations arises mainly from the lack of simple closed expressions relating conserved (τ, \vec{S}, D) and primitive (p, \vec{v}, ρ) variables. This requires the primitive variables to be computed from the conserved variables by a nonlinear iteration.

Among others, Noble et al. (2006) studied several algorithms to convert conserved to primitive variables for the case of a $\tilde{\gamma}$ -law EOS. Ryu et al. (2006), for the EOS defined in Equation (21), applied a Newton–Raphson method (NRM) to an 8th-order equation dependent on Γ . Mignone & McKinney (2007), for the case of relativistic MHD with a general EOS, derived an equation for $W = D\rho h$ and evaluated W by a

Newton–Raphson iterative scheme, with the derivative dW/dp given by using thermodynamic relations. Here, we present a different implementation. Taking advantage of the existence of a relation between the specific enthalpy h and $\Theta = p/(\rho c^2)$, we solve the system of Equations (4)–(6) as a function of Θ by using a standard NRM, and we then determine the other variables.

First, squaring the momentum equation ($S_k = Dh\Gamma v_k$) we get

$$\Gamma^2 = 1 + \frac{S^2}{D^2 h^2}, \quad (22)$$

with $h = h(\Theta)$. From the definition of specific enthalpy it follows that $h \geq 1$. Therefore, Equation (22) leads to the following inequality (e.g., Schneider et al. 1993):

$$1 \leq \Gamma^2 \leq 1 + \frac{S^2}{D^2}. \quad (23)$$

By using the relation $p = D\Theta c^2/\Gamma$, we can then derive from the definition of energy density (excluding rest mass, i.e., $\tau = Dh\Gamma c^2 - p - Dc^2$) the following identity:

$$f(\Theta) = h(\Theta)\Gamma(\Theta) - \frac{\Theta}{\Gamma(\Theta)} - 1 - \frac{\tau}{Dc^2} = 0. \quad (24)$$

Equations (22) and (24) are then used, together with a standard NRM, to determine Θ , with $df/d\Theta$ given by

$$\frac{df(\Theta)}{d\Theta} = \frac{h'}{\Gamma} \left(1 - \frac{\Theta}{h} \frac{\Gamma^2 - 1}{\Gamma^2} \right) - \frac{1}{\Gamma}, \quad (25)$$

where the relation $\Gamma' = -h'(\Gamma^2 - 1)/(h\Gamma)$ has been used (derived from Equation (22)), and $h' = dh/d\Theta$. The derivative $dh/d\Theta$ depends on the particular EOS used and can be determined both analytically and numerically. In the case of the Ryu et al. (2006) EOS (Equation (21)), $h' = 4 - 6/(3\Theta + 2)^2$.

We also note that $df(\Theta)/d\Theta > 0$ for every value of Θ (for the EOS considered here). Therefore, as $f(\Theta \rightarrow \infty) > 0$, a solution for the equation $f(\Theta) = 0$ exists if $f(\Theta = 0) < 0$, which implies that the relation

$$D^2 + S^2 < (D + \tau/c^2)^2 \quad (26)$$

must hold in order to allow a solution with physically acceptable values of Γ and p (that is, real values of $\Gamma \geq 1$ and $p \geq 0$).

As we have shown, this method can be easily applied to any EOS of the form $h = h(\Theta)$. Furthermore, the guess used by the NRM is provided by simply assuming $\Theta = 0$. In this case, setting a tolerance of 10^{-10} into the Newton–Raphson solver, the method converges typically within ~ 5 iterations. In very rare cases when the NRM fails to converge, a bisection method is used instead.

2.6. Adaptive Mesh Refinement

We have implemented the SRHD equations in the framework of the AMR code Mezcald. In the code, a basic Cartesian grid is built at the beginning of the simulation, and it is refined based on the initial conditions and the subsequent evolution of the flow. The uniform version of the code has been used in the past to simulate MHD jets (e.g., De Colle & Raga 2005, 2006; De Colle et al. 2008).

In the Mezcald code, the computational grid is divided in “octs” (or blocks) of $2^{n_{\text{dim}}}$ cells, where n_{dim} is the number of

dimensions of the problem. Each block has a series of pointers to its vertexes, and each vertex has pointers to the octs sharing that particular vertex. In this way, neighbor octs (along both the axes and the diagonal direction) can be easily located in the grid, facilitating the computation of the MHD solver (which, in staggered mesh methods, is based on determining electric fields at the cell vertexes). At a given time, each position on the grid is covered by only one cell, i.e., there are no pointers between “parent” and “sibling” usually present in other tree-AMR codes (e.g., Berger & Olinger 1984; Khokhlov 1998). Furthermore, there are no ghost cells in any of the blocks. Although the use of pointers causes a small memory overload (corresponding to four integers per cell in three dimensions), that is largely compensated by the fact that, because of the small block size, the grid covers only regions that effectively need to be refined.

At every time step, all blocks are swept, and they are refined/coarsened if a user-defined criterion is fulfilled. Typically, this criterion is based on the first or second derivative of some variable, but more complex criteria can be easily implemented. Once a list of blocks flagged for refinement has been formed, the grid is checked for consistency. As the code maintains a maximum ratio of 2 in the size of neighbor cells, all coarser neighbors of blocks are flagged for refinement. When a block is refined, $2^{n_{\text{dim}}}$ new blocks are created, and the parent block is eliminated. To avoid excessive memory fragmentation, the block lists are periodically reordered.

Coarsening is allowed only when the $2^{n_{\text{dim}}}$ neighbor blocks (previously produced by refining the same parent block) are marked for derefinement during the same time step. We use zeroth-order interpolation when refining and integrate the conserved variables over the volume when coarsening, following the strategy presented by Li & Li (2003).

To evolve the hyperbolic equations, the code employs a time step common to all grid levels. While the use of a global time step may potentially produce an important computational overload (as large as 50%, depending on the problem; see, e.g., Dursi & Zingale 2003) with respect to using a local time step, the local time step method can represent an important bottleneck for parallelization, as blocks on different levels must be evolved sequentially (and not in parallel). The fluxes are computed by locating the neighbor blocks and considering the cells sharing the same faces. When two blocks with different levels of refinement share the same face, $2^{n_{\text{dim}}-1}$ fluxes are computed between the $2^{n_{\text{dim}}-1}$ cells located on the higher level block and the cell part of the block at the lower level of refinement. The fluxes are then added to the conserved variables of the cells sharing the common boundary.

The Mezcald code is parallelized by using the Message Passing Interphase library. The communication time is minimized by scheduling it in parallel with the calculation of the fluxes. This is done by first computing the fluxes between blocks located in each process and then, once the communication phase is completed, computing the rest of the fluxes (between blocks “inside” each process and ghost blocks). The load balancing is achieved by ordering the blocks by a space-filling curve (Sagan 1994), dividing the total number of blocks between the different processes, and moving blocks between unbalanced processes. In the code, the Morton and the Hilbert space-filling curves (Sagan 1994) are implemented. The load balancing is typically applied every ~ 10 time steps and represents an overload of $\sim 1\%$ of the total computational time. The parallel scaling of the AMR code is under evaluation and will be presented elsewhere.

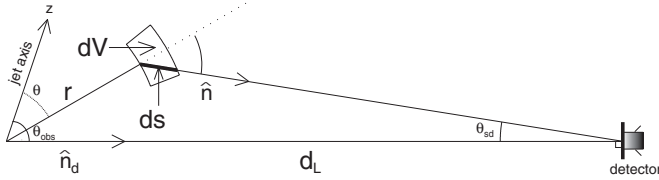


Figure 1. Contribution of a volume element dV to the flux observed by a distant observer is $dF_v(\hat{n}_d) = I_v(\hat{n}) \cos \theta_{sd} d\Omega_{sd} \approx I_v(\hat{n}) d\Omega_{sd}$, where θ_{sd} is the angle between the direction opposite to that at which the detector is pointing ($\hat{n}_d = \hat{Z}$ in the figure) and the local direction from a small emitting region within the source (of volume dV) to the detector. Since the observer is far away, the direction of emission in the observer frame is almost parallel to the z -axis.

3. CALCULATION OF THE EMITTED RADIATION FROM A HYDRODYNAMIC SIMULATION

3.1. Calculation of the Observed Flux Density

Here we provide a detailed derivation of the procedure required to calculate the radiation emitted from a relativistic source, following Granot & Ramirez-Ruiz (2010), which is based on previous work (Granot et al. 1999a, 1999b; Granot & Königl 2003; Kumar & Granot 2003).

The geometry of the problem is shown in Figure 1. We denote with θ_{sd} the angle subtended by the direction \hat{n}_d of the observer (perpendicular to the differential area dA at the detector and opposite to the direction at which the detector is pointing) and the local direction \hat{n} from the relevant (contributing) part of the source to the observer. In practice almost always $\theta_{sd} \ll 1$, as the source size is much smaller than the distance from the source to the observer, so that $\cos \theta_{sd} \approx 1$. We also define $d\Omega_{sd} = d\phi_{sd} d\cos \theta_{sd}$ as the differential solid angle subtended by the contributing portion of the source as viewed by the observer. Our aim is to calculate the observed flux density, $F_v = dE/dAdvdt$, which is the energy per unit area, frequency, and time in the direction \hat{n}_d normal to dA . From the definition of the angular distance to the source, $d_A(z)$, where z is the cosmological redshift, we have $d\Omega_{sd} = dS_{\perp}/d_A^2$, where dS_{\perp} is the differential area in the plane of the sky (normal to \hat{n}) sustained by the source. The angular distance to the source is related to the luminosity distance, $d_L(z)$, by $d_A = (1+z)^{-2}d_L$.

The differential contribution to the flux can be written as $dF_v(\hat{n}_d) = I_v(\hat{n}) \cos \theta_{sd} d\Omega_{sd} \approx I_v(\hat{n}) d\Omega_{sd} = I_v dS_{\perp}/d_A^2$. Here, $I_v(\hat{n}) = dE/dAd\Omega dvdt$ is the specific intensity (the energy per unit area, time, and frequency of radiation directed within a small solid angle $d\Omega$, which is centered on the direction \hat{n}) and should be evaluated at the location of the observer.

For an optically thin source $I_{v_z} = \int j_{v_z} ds_z$, where $j_{v_z} = dE_z/dV_z d\Omega_z dv_z dt_z$ is the emitted energy per unit volume, solid angle, frequency, and time, while ds_z is the differential path length along the trajectory of a photon that reaches the observer at the time t_{obs} when F_v is measured (the subscript z here denotes quantities measured in the cosmological frame of the source). Since I_v/v^3 , j_v/v^2 , and ds/v are Lorentz invariant (Rybicki & Lightman 1979), we have $I_v = (v/v_z)^3 I_{v_z} = (1+z)^{-3} \int j_{v_z} ds_z$. Therefore, $dF_v(\hat{n}_d) = I_v dS_{\perp}/d_A^2 = j_{v_z} dV_z (1+z)/d_L^2$, where $dV_z = dS_{\perp} ds_z$ is the volume element in the source cosmological frame. Here, $j_{v_z} = [\Gamma(1 - \hat{n} \cdot \vec{\beta})]^{-2} j'_{v'}$ is measured in the source (cosmological) frame, while $j'_{v'}$ is measured in the (comoving) rest frame of the emitting material, which expands at a velocity

$\vec{\beta}c$ in the source frame. Altogether, this gives⁶

$$F_v(t_{obs}, \hat{n}) = \frac{(1+z)}{d_L^2(z)} \int d^4x \delta \left(t_z - \frac{\hat{n} \cdot \vec{r}}{c} - \frac{t_{obs}}{1+z} \right) \times \frac{j'_{v'}}{\Gamma^2(1 - \hat{n} \cdot \vec{\beta})^2}, \quad (27)$$

where t_z is the coordinate time at the source's cosmological frame,

$$v' = (1+z)\Gamma(1 - \hat{n} \cdot \vec{\beta})v, \quad t_{obs} = (1+z) \left(t_z - \frac{\hat{n} \cdot \vec{r}}{c} \right), \quad (28)$$

and $t_{obs} = 0$ corresponds to a photon emitted at the origin ($\vec{r} = 0$) at $t_z = 0$. Since $d^4x = dt_z dV_z = dt_z dS_{\perp} ds_z = dt_z dS_{\perp} ds'(v_z/v') = dt_z dV'/\Gamma(1 - \hat{n} \cdot \vec{\beta})$ and $4\pi j'_{v'} dV' = dL'_{v'} = 4\pi(dE'/d\Omega' dv' dt')$ is the differential of the isotropic equivalent spectral luminosity in the comoving frame, Equation (27) can be rewritten as

$$F_v(t_{obs}, \hat{n}) = \frac{(1+z)}{4\pi d_L^2(z)} \int dt_z \delta \left(t_z - \frac{\hat{n} \cdot \vec{r}}{c} - \frac{t_{obs}}{1+z} \right) \times \int \frac{dL'_{v'}}{\Gamma^3(1 - \hat{n} \cdot \vec{\beta})^3}. \quad (29)$$

There are two main approaches to calculate F_v from the results of a numerical simulation. The first one relies on numerically calculating I_v along different lines of sight (i.e., trajectories or world lines of photons that reach the observer) and then computing $dF_v = I_v dS_{\perp}/d_A^2$. This was applied in both analytical (Granot et al. 1999b; Granot & Sari 2002, hereafter GS02) and numerical (Salmonson et al. 2006; van Eerten et al. 2010, 2011) calculations. Its main advantages are that it can properly handle the optically thick regime, where the radiative transfer equation is solved (analytically or numerically) along each line of sight, and that it provides the observed image of the source (i.e., I_v on the plane of the sky) as a by-product, since it is used when calculating F_v . Its main disadvantage for numerical simulations is that it requires accessing many different “snapshots” of the simulation results, corresponding to different lab frame times t_z , for calculating each value of I_v , as it requires integration along the trajectories (or world lines) of photons that reach the observer. The second approach, which we adopt here, avoids this difficulty and was already used in several previous studies (Granot et al. 2001, 2002; Granot & Königl 2003; Kumar & Granot 2003; Nakar & Granot 2007; Zhang & MacFadyen 2009). In this approach the range of observed times, t_{obs} , is divided into a finite number (N_t) of time bins of width $\Delta t_{obs,i}$ centered on $t_{obs,i}$ (for $i = 1, \dots, N_t$). That is, the i th bin corresponds to $t_{obs,i} - \Delta t_{obs,i}/2 < t_{obs} < t_{obs,i} + \Delta t_{obs,i}/2$, and there are no overlaps or gaps, so that $t_{obs,i} + \Delta t_{obs,i}/2 = t_{obs,i+1} - \Delta t_{obs,i+1}/2$ for $1 \leq i \leq N_t - 1$. For many physical systems (such as the ones we simulate), it is convenient to choose logarithmically spaced bins, with a constant $\Delta t_{obs,i}/t_{obs,i}$. If the time bins are sufficiently densely spaced, such that the second time derivative (with respect to t_{obs}) of F_v is correspondingly

⁶ Since $\theta_{sd} \ll 1$, we make the approximation that $\hat{n}_d \approx \hat{n}$ and replace $F_v(t_{obs}, \hat{n}_d)$ with $F_v(t_{obs}, \hat{n})$, for simplicity. As long as $\theta_{sd} \ll \Gamma^{-1}$ (which is also typically the case, in particular for cosmological GRBs), one can also neglect the change in \hat{n} between the different parts of the source and replace \hat{n} with the constant \hat{n}_d .

small, then $F_v(t_{\text{obs},i}, \hat{n})$ can be approximated by its average value within the i th time bin,

$$F_v(t_{\text{obs},i}, \hat{n}) = \frac{1}{\Delta t_{\text{obs},i}} \int_{\Delta t_{\text{obs},i} - \Delta t_{\text{obs},i}/2}^{\Delta t_{\text{obs},i} + \Delta t_{\text{obs},i}/2} dt_{\text{obs}} F_v(t_{\text{obs}}, \hat{n}). \quad (30)$$

Now given that $\delta[f(x - x_0)] = \delta(x - x_0)/|f'(x_0)|$ when $f(x)$ has a single root at x_0 , we obtain

$$\begin{aligned} F_v(t_{\text{obs},i}, \hat{n}) &= \frac{(1+z)}{d_L^2(z)\Delta t_{\text{obs},i}} \int d^4x \int_{\Delta t_{\text{obs},i} - \Delta t_{\text{obs},i}/2}^{\Delta t_{\text{obs},i} + \Delta t_{\text{obs},i}/2} dt_{\text{obs}} \delta \\ &\quad \times \left(\frac{t_{\text{obs}}}{1+z} - t_z + \frac{\hat{n} \cdot \vec{r}}{c} \right) \frac{j'_{v'}}{\Gamma^2(1 - \hat{n} \cdot \vec{\beta})^2} \\ &= \frac{(1+z)^2}{d_L^2(z)\Delta t_{\text{obs},i}} \int d^4x H \left(\frac{\Delta t_{\text{obs},i}}{2(1+z)} - \left| \frac{t_{\text{obs},i}}{1+z} - t_z + \frac{\hat{n} \cdot \vec{r}}{c} \right| \right) \\ &\quad \times \frac{j'_{v'}}{\Gamma^2(1 - \hat{n} \cdot \vec{\beta})^2} \\ &= \frac{(1+z)}{d_L^2(z)\Delta t_{\text{obs},z,i}} \int d^4x H \left(\frac{\Delta t_{\text{obs},z,i}}{2} - \left| t_{\text{obs},z,i} - t_z + \frac{\hat{n} \cdot \vec{r}}{c} \right| \right) \\ &\quad \times \frac{j'_{v'}}{\Gamma^2(1 - \hat{n} \cdot \vec{\beta})^2}, \end{aligned} \quad (31)$$

where $H(x)$ is the Heaviside step function and $t_{\text{obs},z} \equiv t_{\text{obs}}/(1+z)$.

The results of a simulation that models the dynamics of a physical system are naturally given at a finite number (n_t) of time steps ($t_{z,j}$, where $j = 1, \dots, n_t$), i.e., ‘‘snapshots’’ of the dynamics. At each snapshot the values of the hydrodynamic variables are provided at a finite number of points, each at the center of a computational cell, which represents a finite three-dimensional (3D) volume $\Delta V^{(3)}$ (generally different from that of other cells for an AMR code). For this reason, we assign to each snapshot time $t_{z,j}$ a finite time interval: $(3t_{z,1} - t_{z,2})/2 < t_z < (t_{z,1} + t_{z,2})/2$ and $\Delta t_{z,1} = t_{z,2} - t_{z,1}$ for $j = 1$, $(t_{z,j-1} + t_{z,j})/2 < t_z < (t_{z,j} + t_{z,j+1})/2$ and $\Delta t_{z,j} = (t_{z,j+1} - t_{z,j-1})/2$ for $2 \leq j \leq n_t - 1$, and $(t_{z,n_t-1} + t_{z,n_t})/2 < t_z < (3t_{z,n_t} - t_{z,n_t-1})/2$ and $\Delta t_{z,n_t} = t_{z,n_t} - t_{z,n_t-1}$ for $j = n_t$. Sufficiently dense and well-distributed snapshot times are key to the flux calculations. Thus, the simulation provides a finite number of four-dimensional (4D) space-time cells, which together cover the finite simulated 4-volume (the time and 3D volume covered by the simulation⁷). The 4-volume of the k th 3D cell of the j th snapshot time is $\Delta V_{jk}^{(4)} = \Delta t_{z,j} \Delta V_{jk}^{(3)}$. Given the physical conditions in each such 4D space-time cell, we can then calculate its local (comoving) emissivity, $j'_{v'}$ (under appropriate assumptions), and use Equation (31) in order to calculate its contribution to the observed flux density, F_v . The proper way of doing this is to calculate the fraction f_{ijk} of its 4-volume $\Delta V_{jk}^{(4)}$ that falls within each observer time bin centered on $t_{\text{obs},i}$, resulting in the following discretized version of Equation (31):

$$F_v(t_{\text{obs},i}, \hat{n}) = \frac{(1+z)^2}{d_L^2(z)\Delta t_{\text{obs},i}} \sum_{j,k} f_{ijk} \Delta V_{jk}^{(4)} \frac{j'_{v',jk}}{\Gamma^2(1 - \hat{n} \cdot \vec{\beta}_{jk})^2}, \quad (32)$$

where the subscript ‘‘ jk ’’ indicates that the relevant quantities are evaluated at the appropriate cell, centered on $(t_z, \vec{r}) = (t_{z,j}, \vec{r}_{jk})$.

⁷ Note that usually even in a 1D or 2D simulation represents a 3D volume given the relevant assumed symmetry of the problem.

Since the order of the summation is not important, it is much more convenient to evaluate the contributions of each 4D cell according to the order at which it is stored. Since it is not always convenient and may cost additional computational time to calculate all of the coefficients f_{ijk} , one might further simplify Equation (32) by attributing all of the contribution from any given 4D cell to a single observer time interval, corresponding to that of the cell’s center:

$$\begin{aligned} \Delta F_{v,i,jk}(\hat{n}) &= \frac{(1+z)^2}{d_L^2(z)} \frac{\Delta V_{jk}^{(4)}}{\Delta t_{\text{obs},i}} \frac{j'_{v',jk}}{\Gamma_{jk}^2(1 - \hat{n} \cdot \vec{\beta}_{jk})^2} \\ &\quad \text{for } \left| \frac{t_{\text{obs},i}}{1+z} - t_{z,j} + \frac{\hat{n} \cdot \vec{r}_{jk}}{c} \right| < \frac{\Delta t_{\text{obs},i}}{2(1+z)} \\ &= \frac{(1+z)}{d_L^2(z)} \frac{\Delta V_{jk}^{(4)}}{\Delta t_{\text{obs},z,i}} \frac{j'_{v',jk}}{\Gamma_{jk}^2(1 - \hat{n} \cdot \vec{\beta}_{jk})^2} \\ &\quad \text{for } \left| t_{\text{obs},z,i} - t_{z,j} + \frac{\hat{n} \cdot \vec{r}_{jk}}{c} \right| < \frac{\Delta t_{\text{obs},z,i}}{2}. \end{aligned} \quad (33)$$

Finally, one could simplify things even further by assuming an isotropic emission in the fluid (comoving) rest frame, and then $j'_{v'}(\hat{n}') = dE'/dV'd\Omega'dv'dt'$ can be replaced by $P'_{v'}/4\pi$, where $P'_{v'} = dE'/dV'dv'dt'$. We currently make this simplifying assumption.

For 2D jet simulations, which assume an axisymmetric flow, the jet symmetry axis is the z -axis and it is convenient to choose the x -axis along the \hat{n} - \hat{z} plane, so that \hat{n} may be easily expressed in terms of the viewing angle θ_{obs} (where $\cos \theta_{\text{obs}} = \hat{n} \cdot \hat{z}$),

$$\hat{n} = \hat{x} \sin \theta_{\text{obs}} + \hat{z} \cos \theta_{\text{obs}}. \quad (34)$$

Thus, in spherical (r, θ, ϕ) or cylindrical (z, ρ, ϕ) coordinates (with $\beta_\phi = 0$), we have

$$\begin{aligned} \hat{n} \cdot \vec{r} &= r(\sin \theta \cos \phi \sin \theta_{\text{obs}} + \cos \theta \cos \theta_{\text{obs}}) \\ &= \rho \cos \phi \sin \theta_{\text{obs}} + z \cos \theta_{\text{obs}}, \\ \hat{n} \cdot \vec{\beta} &= (\beta_r \sin \theta + \beta_\theta \cos \theta) \cos \phi \sin \theta_{\text{obs}} \\ &\quad + (\beta_r \cos \theta - \beta_\theta \sin \theta) \cos \theta_{\text{obs}} \\ &= \beta_\rho \cos \phi \sin \theta_{\text{obs}} + \beta_z \cos \theta_{\text{obs}}. \end{aligned} \quad (35)$$

3.2. Calculation of the Observed Image

The observed image can be calculated by dividing the plane of the sky (i.e., the plane normal to \hat{n}) into bins or 2D ‘‘pixels’’ and assigning the contribution $\Delta F_{v,jk}$ from each computational 4D cell to the appropriate pixels (or pixel), where the conversion from flux to specific intensity (which is relevant for the image calculation) is done by using the relation $dF_v = I_v dS_{\perp}/d_A^2$, so that the intensity contribution to the l th pixel whose area is $\Delta S_{\perp,l}$ would be

$$\begin{aligned} \Delta I_{v,il,jk}(\hat{n}) &= d_A^2 \frac{\Delta F_{v,i,jk}(\hat{n})}{\Delta S_{\perp,l}} = \frac{(1+z)^{-2} \Delta V_{jk}^{(4)}}{\Delta S_{\perp,l} \Delta t_{\text{obs},i}} \frac{j'_{v',jk}}{\Gamma_{jk}^2(1 - \hat{n} \cdot \vec{\beta}_{jk})^2} \\ &= \frac{(1+z)^{-3} \Delta V_{jk}^{(4)}}{\Delta S_{\perp,l} \Delta t_{\text{obs},z,i}} \frac{j'_{v',jk}}{\Gamma_{jk}^2(1 - \hat{n} \cdot \vec{\beta}_{jk})^2}. \end{aligned} \quad (36)$$

The assignment of the contribution to the appropriate pixel requires a parameterization of the plane of the sky. For this purpose we use a rotated reference frame denoted by a twiddle,

where $\tilde{y} = y$ and the \tilde{z} -axis points to the observer (in the direction of \hat{n}),

$$\begin{aligned}\tilde{x} &= x \cos \theta_{\text{obs}} - z \sin \theta_{\text{obs}} \\ &= r(\sin \theta \cos \phi \cos \theta_{\text{obs}} - \cos \theta \sin \theta_{\text{obs}}) \\ &= \rho \cos \phi \cos \theta_{\text{obs}} - z \sin \theta_{\text{obs}}, \\ \tilde{y} &= y = r \sin \theta \sin \phi = \rho \sin \phi, \quad \tilde{\rho} = \sqrt{\tilde{x}^2 + \tilde{y}^2}, \quad (37) \\ \tan \tilde{\phi} &= \frac{\tilde{y}}{\tilde{x}} = \frac{\sin \theta \sin \phi}{\sin \theta \cos \phi \cos \theta_{\text{obs}} - \cos \theta \sin \theta_{\text{obs}}} \\ &= \frac{\rho \sin \phi}{\rho \cos \phi \cos \theta_{\text{obs}} - z \sin \theta_{\text{obs}}}.\end{aligned}$$

For an axisymmetric flow the image is invariant to $\tilde{y} \rightarrow -\tilde{y}$ or equivalently to $\tilde{\phi} \rightarrow -\tilde{\phi}$, i.e., $I_\nu(t_{\text{obs}}, \hat{n}, \tilde{x}, \tilde{y}) = I_\nu(t_{\text{obs}}, \hat{n}, \tilde{x}, -\tilde{y})$ and $I_\nu(t_{\text{obs}}, \hat{n}, \tilde{\rho}, \tilde{\phi}) = I_\nu(t_{\text{obs}}, \hat{n}, \tilde{\rho}, -\tilde{\phi})$.⁸ A 2D simulation (whether in spherical or cylindrical coordinates) provides 2D snapshots of the dynamics, and each 2D computational cell (not counting the time dimension) needs to be transformed into one or more 3D cells. For the special case of an observer along the jet (or flow) symmetry axis, corresponding to $\theta_{\text{obs}} = 0$, the contribution to the observed emission (i.e., to I_ν or F_ν) becomes independent of $\tilde{\phi}$, which in this case is equal to ϕ , so that the image has circular symmetry (I_ν becomes independent of $\tilde{\phi}$) and a single bin in ϕ becomes sufficient for the calculation. For $\theta_{\text{obs}} > 0$, however, one needs to artificially produce a large number of bins in ϕ , each corresponding to a 3D cell, which together represent a single 2D computational region. The choice of binning should be done wisely, such that the Doppler factor does not vary by a large factor between neighboring bins (in order to calculate the observed radiation accurately enough), and the bin size should not be too coarse (as to cause excessive graininess in the calculated images or light curves), while having a reasonable number of bins (in order for the computational time not to be too large, especially for high-resolution simulations). Please note that since the contribution to the flux is invariant to $\phi \rightarrow -\phi$, it is enough to choose values in the range $0 < \phi < \pi$ and give each resulting 3D or 4D cell a double weight when calculating F_ν (since $\phi_1 < \phi < \phi_2$ also represents $-\phi_2 < \phi < -\phi_1$).

3.3. Synchrotron Radiation

The main purpose of the current radiation calculations is to check the effect of the dynamics on the afterglow light curves. Because of this, we intentionally use a very simple model for the radiation mechanism (following Granot et al. 1999a), which features synchrotron emission and ignores inverse Compton scattering or its effects on the synchrotron emission through the additional electron cooling that it causes. It also ignores self-absorption, and the local emission spectrum is approximated by a broken power law. The magnetic field is assumed to hold everywhere a fraction ϵ_B of the proper internal energy density, e' , i.e., $B^2/8\pi = \epsilon_B e'$. Just behind the shock all electrons are assumed to be accelerated into a power-law energy distribution,

$$N(\gamma_e) \propto \gamma_e^{-p} \quad \text{for} \quad \gamma_e > \gamma_m = \left(\frac{p-2}{p-1} \right) \frac{\epsilon_e e'}{n_e m_e c^2}. \quad (38)$$

⁸ This can also be seen from Equation (35), where the dependence on ϕ is only through $\cos \phi$, which is invariant to $\phi \rightarrow -\phi$, which, according to Equation (37), corresponds to $\tilde{y} \rightarrow -\tilde{y}$ or $\tilde{\phi} \rightarrow -\tilde{\phi}$.

The local emissivity $P'_{\nu'}$ is taken to be a broken power law,

$$\frac{P'_{\nu'}}{P'_{\nu', \text{max}}} = \begin{cases} (v'/v'_m)^{1/3} & v' < v'_m < v'_c, \\ (v'/v'_c)^{1/3} & v' < v'_c < v'_m, \\ (v'/v'_m)^{(1-p)/2} & v'_m < v' < v'_c, \\ (v'/v'_c)^{-1/2} & v'_c < v' < v'_m, \\ (v'/v'_m)^{(1-p)/2} (v'/v'_c)^{-1/2} & v' > \max(v'_m, v'_c), \end{cases} \quad (39)$$

with the following flux normalization and break frequencies:

$$P'_{\nu', \text{max}} = 0.88 \frac{512 \sqrt{2\pi}}{27} \left(\frac{p-1}{3p-1} \right) \frac{q_e^3}{m_e c^2} (\epsilon_B e')^{1/2} n_e', \quad (40)$$

$$v'_m = \frac{3\sqrt{2\pi}}{8} \left(\frac{p-2}{p-1} \right)^2 \frac{q_e}{m_e^2 c^5} \epsilon_B^{1/2} \epsilon_e^2 (e')^{5/2} (n_e')^{-2}, \quad (41)$$

$$v'_c = \frac{27\sqrt{2\pi}}{128} \frac{q_e m_e c}{\sigma_T^2} (\epsilon_B e')^{-3/2} \left(\frac{\Gamma}{t_z} \right)^2. \quad (42)$$

Electron cooling is treated in an approximate manner, by assuming that everywhere the electrons have cooled at their current local cooling rate over the dynamical time, which is in turn approximated as $t'_{\text{dyn}} \approx t_z/\Gamma$, so that the expression in Equation (42) is simply derived from

$$\gamma_c = \frac{3m_e c}{4\sigma_T \epsilon_B e' t'_{\text{dyn}}} \approx \frac{3m_e c \Gamma}{4\sigma_T \epsilon_B e' t_z}, \quad v'_c = \frac{3q_e B' \gamma_c^2}{16m_e c}. \quad (43)$$

A more proper treatment of the electron cooling would require following each fluid element from the point where it crosses the shock and the electrons are accelerated and solving the equation for the subsequent evolution of their energy distribution, accounting for their radiative losses and adiabatic gains or losses. This has been done analytically for the BMK self-similar solution (Granot & Sari 2002) and numerically using a 1D Lagrangian code (Nakar & Granot 2007). It has also been implemented in a Eulerian code (van Eerten et al. 2010, 2011), in a somewhat approximate fashion as a result of the difficulty in accurately tracking the electron energy distribution in each fluid element. The differences between our treatment of the electron cooling and the results presented by Granot & Sari (2002) are shown in detail in Appendix A.

It is also possible to use an even simpler emission model that ignores electron cooling altogether by assuming $v', v'_m < v'_c$ in the broken power laws of Equations (39). In this paper electron cooling is always implemented in our calculations. In an accompanying paper (De Colle et al. 2011), however, in some cases we also use an even simpler emission model that ignores electron cooling altogether,

$$\frac{P'_{\nu'}}{P'_{\nu', \text{max}}} = \begin{cases} (v'/v'_m)^{1/3} & v' < v'_m, \\ (v'/v'_m)^{(1-p)/2} & v' > v'_m. \end{cases} \quad (44)$$

4. APPLICATION: EVOLUTION OF A RELATIVISTIC IMPULSIVE BLAST WAVE

In this section, we use our AMR+radiation code to study the evolution of impulsive relativistic blast waves both in 1D (a spherical blast wave propagating into either a uniform or a stratified medium, bridging from the Blandford–McKee to the Sedov–Taylor (ST) self-similar solutions) and in 2D (an axisymmetric jet propagating into a uniform medium).

4.1. Self-similar Solution

Blandford & McKee (1976) studied the self-similar propagation of an ultrarelativistic spherical impulsive blast wave in a medium with a density

$$\rho_k(r) = A_k r^{-k}. \quad (45)$$

They showed that an appropriate choice of the similarity variable is

$$\chi = 1 + 2(4 - k)\Gamma_{\text{sh}}^2 \left(1 - \frac{r}{R}\right), \quad (46)$$

where r and R are the radial positions (in polar coordinates) of the fluid element and of the shock front, respectively; Γ_{sh} is the Lorentz factor of the shock front, which, as that of the fluid (and all of the velocities), here is measured in the rest frame of the upstream medium ahead of the shock, and it is related to the Lorentz factor of the shocked fluid just behind the shock front by $\Gamma(\chi = 1) = \Gamma_{\text{sh}}/\sqrt{2}$. Blandford & McKee (1976) showed that the position of the shock front is given by

$$R = ct \left[1 - \frac{1}{2(4 - k)\Gamma_{\text{sh}}^2}\right], \quad (47)$$

and its Lorentz factor can be written as

$$\Gamma_{\text{sh}}^2 = \frac{(17 - 4k)E}{8\pi\rho_k(R)c^5 t^3}, \quad (48)$$

where $\rho_k(R) = A_k R^{-k}$ is the density of the ambient (unshocked) medium at the position of the shock front and E is the energy in the blast wave.

The lab frame time corresponding to a given Lorentz factor of the shock front is therefore (see Equations (45), (47), and (48)) given by

$$t \cong \frac{R}{c} \cong \frac{1}{c} \left[\frac{(17 - 4k)E}{8\pi A_k c^2 \Gamma_{\text{sh}}^2} \right]^{1/(3-k)}. \quad (49)$$

The post-shock Lorentz factor Γ , proper rest-mass density ρ , and pressure p are given by

$$\Gamma = \frac{1}{\sqrt{2}} \Gamma_{\text{sh}} \chi^{-1/2}, \quad (50)$$

$$\rho = 2^{3/2} \rho_k(R) \Gamma_{\text{sh}} \chi^{-(10-3k)/[2(4-k)]}, \quad (51)$$

$$p = \frac{2}{3} \rho_k(R) c^2 \Gamma_{\text{sh}}^2 \chi^{-(17-4k)/[3(4-k)]}. \quad (52)$$

The relativistic blast wave typically begins to slow down when it sweeps up an amount of mass with a rest-mass energy of order of the kinetic energy of the blast wave. That corresponds to a distance (Sedov length) of

$$L_S = \left[\frac{(3 - k)E}{4\pi A_k c^2} \right]^{1/(3-k)}, \quad (53)$$

where the jet energy E is the energy (excluding rest energy) in the flow. For a nonspherical flow, or a jet, to zeroth order E in Equations (48) and (49) can be replaced by the local value of the isotropic equivalent energy in the flow, $E_{\text{iso}} = 4\pi(dE/d\Omega)$, as long as it does not vary significantly over an angular scale of the order of the inverse of the local value of the Lorentz factor

of the fluid just behind the shock. In particular, for a double-sided conical wedge of half-opening angle θ_0 taken out of the BMK solution (or a uniform sharp-edged jet), which we later use as the initial conditions of our 2D simulations, we have $E = (1 - \cos \theta_0)E_{\text{iso}} \approx (\theta_0^2/2)E_{\text{iso}} \approx 2 \times 10^{51}(\theta_0/0.2)^2 E_{\text{iso},53}$ erg, where we have used a fiducial value of $E_{\text{iso}} = 10^{53} E_{\text{iso},53}$ erg, typical for long-duration GRBs. Whether it is more appropriate to use E or E_{iso} in Equation (53) for such a jet, i.e., at which distance from the origin it becomes Newtonian, is a nontrivial question, which is addressed in an accompanying paper (De Colle et al. 2011).

In the nonrelativistic limit, the self-similar behavior of the blast wave is described by the ST (Sedov 1959; Taylor 1950) self-similar solution, with the position of the shock wave given by

$$R \approx \left[\frac{\alpha_k E_{\text{iso}} t^2}{A_k} \right]^{1/(5-k)} \quad (54)$$

and the shock velocity given by $v_{\text{sh}} = dR/dt \propto t^{-(3-k)/(5-k)}$. Approximated expressions for the post-shock density, pressure, and velocity profiles in the ST regime are given, e.g., by Petruk (2000). As there are not analytical solutions for the scaling of density, pressure, and velocity in the post-shock region, it is not possible to find a simple analytical expression for α_k . Based on the simulations presented in Section 4.2, we find $\alpha_k^{1/(5-k)} = 1.15, 1.04, 0.78$ for $k = 0, 1, 2$, respectively.

4.2. Initial Conditions

In this paper, we perform a series of 1D (with $k = 0, 1, 2$) and 2D (with $k = 0$) simulations of the propagation of impulsive blast waves, including the transition from the relativistic to the nonrelativistic phase. All simulations employ spherical (polar) coordinates, using the HLL method (see Section 2.2) for the flux calculation. The multi-dimensional simulations for the cases $k = 1, 2$ are presented in an upcoming paper (De Colle et al. 2011).

The initial conditions of the problem depend on the values of the following parameters: the isotropic energy of the blast wave, E_{iso} , the initial Lorentz factor of the jet shock front, $\Gamma_{\text{sh},0}$, the density profile of the external medium (that is, the values of k and of the normalization factor A_k), and the jet initial half-opening angle, θ_0 (in the 2D case). In all the simulations, the initial profiles of density, pressure, and Lorentz factor (radial velocity) in the post-shock region are set from the BMK self-similar solutions, given by Equations (50)–(52). We initialize the density of the ambient medium (in the case $k = 0$) as $A_0 = \rho_0 = n_0 m_p = 1.67 \times 10^{-24}$ g cm⁻³, and the pressure as $p = \eta \rho_0 c^2$, with $\eta = 10^{-10}$. The value of η does not affect the outcome of the simulation as long as the Mach number remains large, i.e., $\mathcal{M} \sim \eta^{-1/2} v_{\text{sh}}/c \gg 1$. As the simulation continues to evolve well into the Newtonian regime, this condition corresponds to $v_{\text{sh}} \gg 3 (\eta/10^{-10})^{1/2}$ km s⁻¹.

In a first set of simulations, we study the deceleration of mildly relativistic impulsive blast waves bridging from the BMK to the ST self-similar solution. In the case $k = 0$, the initial conditions are similar to those used by van Eerten et al. (2010). To determine the density profile in the cases $k = 1, 2$, we fix the Sedov length (Equation (53)) as $L_S(k) = L_S(k = 0)$,

$$L_S = \left[\frac{(3 - k)E}{4\pi A_k c^2} \right]^{1/(3-k)} = \left(\frac{3E}{4\pi A_0 c^2} \right)^{1/3} \quad (55)$$

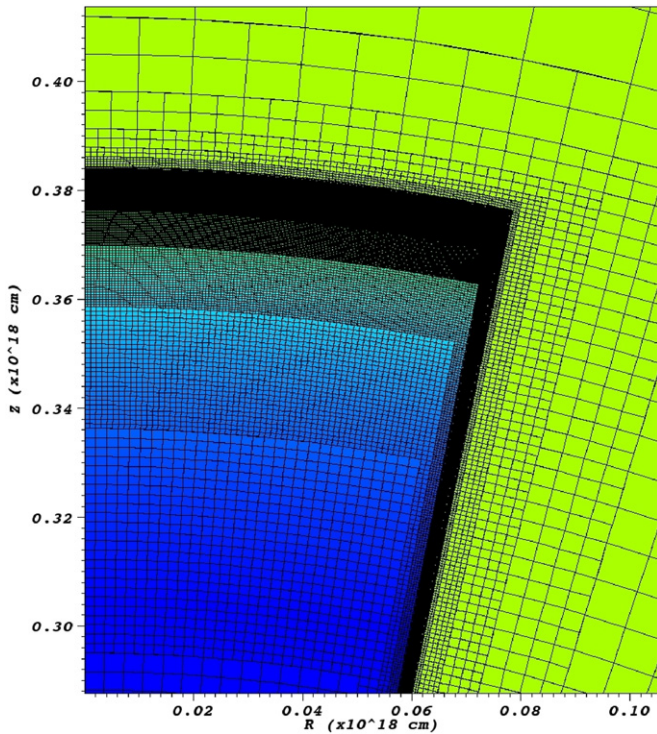


Figure 2. Adaptive grid structure for the initial condition of the two-dimensional simulation of a relativistic blast wave. The blue color indicates the post-shock region, while the green area represents the ambient (unshocked) medium.

(A color version of this figure is available in the online journal.)

and derive an expression for A_k as $A_k = A_0 L_S^k (3 - k)/3$. Therefore,

$$\rho = A_0 \frac{3 - k}{3} \left(\frac{r}{L_S} \right)^{-k}. \quad (56)$$

We further assume $E_{\text{iso}} = 10^{52}$ erg, corresponding to a Sedov length of $L_S = 1.17 \times 10^{18}$ cm and a Lorentz factor of the shock of $\Gamma_{\text{sh},0} = 10$. To properly cover the deceleration to nonrelativistic speeds (especially for the case $k = 2$), we use a large spherical box of radial size $L_r = 3 \times 10^{20}$ cm (corresponding to a size of $\approx 256 L_S$). The simulation is stopped at $t_{\text{fin}} = 500$ yr.

In the case $k = 0$, the simulations begin at $t_0 = 1.19 \times 10^7$ s, with a jet shock located at $R_0 = 3.56 \times 10^{17}$ cm. The case $k = 1$ corresponds to an initial time and jet shock radius given by $t_1/t_0 = R_1/R_0 = 0.53$. The case $k = 2$, corresponding to a steady spherically symmetric wind, has $t_2/t_0 = R_2/R_0 = 0.074$. The values assumed for the spherical wind can be compared with those observed for Wolf-Rayet stars, whose winds have large mass-loss rates of $\dot{M} \approx 10^{-5}$ to $10^{-4} M_\odot \text{ yr}^{-1}$ and velocities $v_w \approx 1000$ – 2500 km s^{-1} (e.g., Chiosi & Maeder 1986), giving $n_w(r) \approx 0.45(r/10^{18} \text{ cm})^{-2} (\dot{M}_{\text{wr}}/3 \times 10^{-5} M_\odot \text{ yr}^{-1})(v_{\text{wr}}/2 \times 10^3 \text{ km s}^{-1}) \text{ cm}^{-3}$, which is very similar to the one used in the simulations.

The AMR code uses a basic grid of 1000 cells with a maximum of 18 levels of refinement, corresponding to a maximum resolution of $\Delta r_{\text{min}} = 2.3 \times 10^{12}$ cm. In a uniform grid code, the same resolution would be achieved by using 1.3×10^8 cells.

In a second set of simulations, we test the radiation code by running simulations of highly relativistic decelerating blast waves (limited to the case $k = 0$) in both 1D and 2D. In these simulations, we assume an isotropic energy of $E_{\text{iso}} = 10^{53}$ erg,

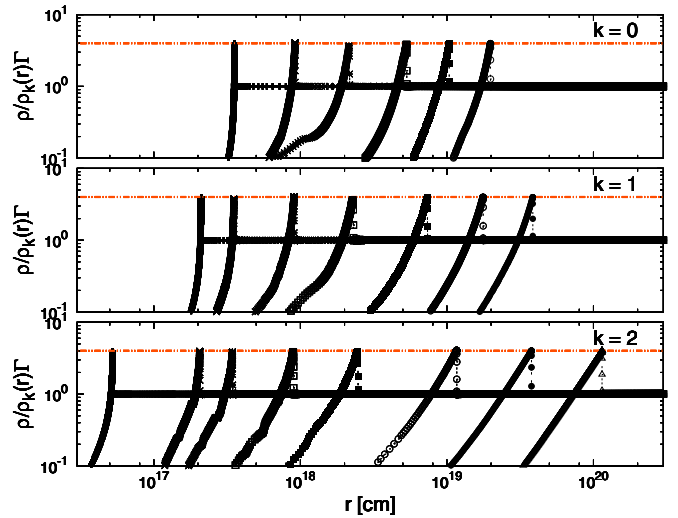


Figure 3. Density profiles normalized to the Lorentz factor and the local value of the ambient medium density. The curves shown in the upper panel ($k = 0$) correspond to $t = t_0 = 137$ days and $t = 1, 3, 20, 100, 500$ yr. The central panel ($k = 1$) includes also the profile at $t_0 = 81$ days. The lower panel ($k = 2$) includes also the profile at $t_0 = 20.3$ days. The horizontal red line indicates $\rho/\rho_k(r)\Gamma = 4$.

(A color version of this figure is available in the online journal.)

corresponding to a Sedov length of $L_S = 2.51 \times 10^{18}$ cm and a Lorentz factor of $\Gamma_{\text{sh},0} = \sqrt{2} \times 20$. The simulations begin at $t_0 = 1.277 \times 10^7$ s, with the shock initially located at $R_0 = 3.83 \times 10^{17}$ cm, and end at $t_{\text{fin}} = 150$ yr. To properly study its lateral expansion, an initial opening angle of $\theta_0 = 0.2$ rad (in the 2D case) is assumed for the jet.

The spherical box has a radial size of $L_r = 1.1 \times 10^{19}$ cm and angular size (in the 2D simulation) $L_\theta = \pi/2$. The AMR code uses a basic grid of 100 cells along the radial direction in both 1D and 2D and 4 cells along the θ direction in the 2D simulations. We run a series of simulations varying the maximum number of refinement levels. The lowest resolution simulation uses 10 maximum levels, while the highest employs 18 levels of refinement in 1D and 15 in 2D, corresponding to a maximum resolution of $\Delta r_{\text{min}} = 2.1 \times 10^{11}$ cm in 1D and $\Delta r_{\text{min}} = 6.7 \times 10^{12}$ cm, $\Delta\theta_{\text{min}} = 2.4 \times 10^{-5}$ rad (along r and θ) in 2D. The structure of the grid at the beginning of the simulation is shown in Figure 2 for the 2D run. In a uniform grid code, the same resolution would be achieved by employing 5.2×10^7 cells in 1D and $\sim 10^{11}$ cells in 2D.

To keep approximately constant the resolution of the relativistic thin shell $\Delta \propto t^{4-k}$, the maximum number of levels of refinement N_{levels} is decreasing with time (Granot 2007) as $N_{\text{levels}} = \max[7, N_{\text{levels},0} - (4 - k) \log(t/t_0)/\log(2)]$. We refine our adaptive mesh based on rest-mass density and energy gradients. The 1D simulations run in at most a few hours on a normal workstation, while the 2D simulations need a few days on ~ 100 processors.

4.3. One-dimensional Simulations of Trans-relativistic Blast Waves Propagating in a Stratified Medium ($k = 0, 1, 2$)

During its deceleration, the shock front is typically resolved with 3–4 cells (Figure 3), as is the case for most modern Eulerian shock capturing schemes. The normalized lab frame density behind the shock, given from the relativistic Rankine–Hugoniot conditions for strong shocks ($\rho/\rho_k(R)\Gamma = (\bar{\gamma} + 1/\Gamma)/(\bar{\gamma} - 1)$), remains approximately constant during the transition from

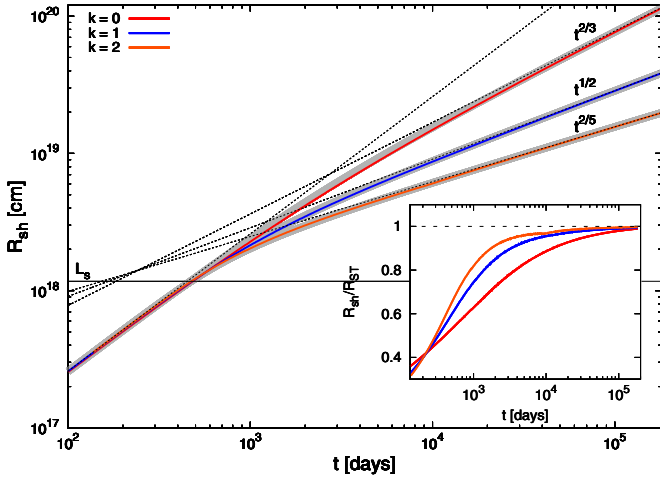


Figure 4. Position of the shock front for the three cases $k = 0, 1, 2$ (top to bottom) along with the ultrarelativistic ($R_{\text{sh}} = ct$) and the ST ($R_{\text{sh}} = (\alpha_k E_{\text{iso}} t^2 / A_k)^{1/(5-k)}$) regimes. The ST curves assume $\alpha_k^{1/(5-k)} = 1.15, 1.04, 0.78$ for $k = 0, 1, 2$, respectively. The gray curves are computed from a semianalytical approximation based on energy conservation (see the text for a detailed description).

(A color version of this figure is available in the online journal.)

relativistic to nonrelativistic regimes (see, e.g., Beloborodov & Uhm 2006; van Eerten et al. 2010). Figure 3 shows that in fact $\rho/\rho_k(R)\Gamma \approx 4$ at different times and for different values of k . The drop of the density profile in the post-shock region approximately follows the BMK self-similar solution and is therefore less steep with larger k (see Equation (51)). This figure also shows that the deceleration process is slower for a more stratified medium.

Figure 4 shows the evolution of the shock front radius for different density stratifications. Both the ultrarelativistic (with $R_{\text{sh}} \approx ct$) and the nonrelativistic ($R \propto t^{2/(5-k)}$) analytical self-similar solutions are properly recovered by the simulations. As shown, e.g., by van Eerten et al. (2010) for the case $k = 0$, the transition from relativistic to nonrelativistic phase happens on scales much larger than L_s . If, for instance, we estimate from Figure 4 the time it takes for the relativistic blast wave to slow down to nonrelativistic speeds based on the intersection between the relativistic and nonrelativistic self-similar curves, we obtain values of $\sim 0.9 \times 10^3$, 1.2×10^3 , and 2.7×10^3 days for $k = 0, 1$, and 2 , respectively. These values are much larger than those computed by using the Sedov length (Piran 2005b), $t_{\text{NR}} \sim L_{\text{NR}}/c = 450$ days.

This result, together with the scaling of position, Lorentz factor, and the shock velocity as a function of time and shock radius, can be easily understood by a simple analytical argument involving the conservation of energy. In fact, the energy is given in the ultrarelativistic regime by

$$E = \frac{8\pi}{17-4k} A_k c^2 R^{3-k} \Gamma^2 \beta^2 \quad (57)$$

and in the nonrelativistic limit by

$$E = \frac{(5-k)^2}{4\alpha_k} A_k v^2 R^{3-k}. \quad (58)$$

As the energy has a common scaling in relation with the other physical parameters (v , R), differing only in the constant of proportionality, a simple interpolation between the two limits is

given by

$$E = R^{3-k} \beta^2 \Gamma^2 A_k c^2 \left[\frac{8\pi}{17-4k} \beta^2 + \frac{(5-k)^2}{4\alpha_k} (1-\beta^2) \right]. \quad (59)$$

This equation can be easily written as a function of velocity as

$$\beta^2 = \frac{2}{1 + c_{\text{NR}}(R/L_s)^{3-k} + \sqrt{[1 - c_{\text{NR}}(R/L_s)^{3-k}]^2 + 4c_R(R/L_s)^{3-k}}}, \quad (60)$$

where $c_R = (2(3-k))/(17-4k)$ and $c_{\text{NR}} = ((5-k)^2(3-k))/16\pi\alpha_k$. This expression approximately gives the dependence of v (or Γ) on the shock position, for every choice of the blast wave energy and density stratification. For instance, at $R \sim L_s$, Equation (60) gives $v_{\text{sh}} \sim 0.83, 0.85, 0.89c$ (or $u = \Gamma\beta \sim 1.46, 1.64, 1.99$) for $k = 0, 1, 2$, respectively. At this radius (and time) the shock is therefore still relativistic, and the ST solution is not valid. The exact determination of t_{NR} depends, however, on the definition of the transition between the relativistic and the nonrelativistic flow (e.g., Ramirez-Ruiz & MacFadyen 2010). If, for instance, we define t_{NR} as the time in which the asymptotic BMK solution and the ST power laws are equal (i.e., $ct/L_s = [4\pi\alpha_k/(3-k)]^{1/(3-k)}$), we get $t \sim 2.1t_{\text{NR}} \sim 9 \times 10^2$ days ($k = 0$), $t \sim 3t_{\text{NR}} \sim 3.4$ yr ($k = 1$), and $t \sim 6t_{\text{NR}} \sim 7.5$ yr ($k = 2$). At this time the blast wave is nonetheless still mildly relativistic ($\beta = 0.51, 0.56, 0.63$) and the ST solution is not valid. If, on the other hand, we assume that the ST solution becomes valid at a fixed (somehow arbitrary) speed of $v/c \lesssim 1/3$, we get $t \sim 3.6t_{\text{NR}} \sim 1.6 \times 10^3$ days ($k = 0$), $t \sim 7t_{\text{NR}} \sim 8.6$ yr ($k = 1$), and $t \sim 48t_{\text{NR}} \sim 59$ yr ($k = 2$) (Figure 4).

Equation (60), when rewritten in the form $dR/dt = \beta(R)$, admits a complex solution $t = f(R)$ in terms of Appell hypergeometric functions. The time dependence of the shock position $R = R(t)$ has been therefore more easily derived by numerically integrating Equation (60), and it approximates the position of the shock computed from the numerical simulation within a maximum difference of 1%, 2%, 5% (for $k = 0, 1, 2$, respectively).

While Figures 3 and 4 clearly show the validity of our implementation for mildly relativistic and nonrelativistic speeds, reproducing the correct BMK self-similar scaling during the early stages of the simulation, when $\Gamma \gtrsim 10$, is much more challenging.

Figure 5 shows the initial density profile (for the case $k = 0$) in the region around the position of the shock. A very large number of levels of refinement must be used to properly initialize the density, pressure, and Lorentz factor in the post-shock region. For instance (Figure 5, upper panel), the initial steep density profile is recovered with errors less than 10% only by using resolutions corresponding to $\gtrsim 18$ levels of refinement.

While the BMK self-similar solution represents an exact solution of the SRHD equations in the ultrarelativistic limit, the particular discretization employed may not be the exact (numerical) solution of the discretized equations. As a consequence, the relaxation toward the numerical solution passes through the development (see Figure 5, lower panel) of a spurious numerical ‘‘precursor’’ propagating in front of the BMK shock if insufficient resolution is used. While the size of the precursor shock drops effectively with resolution, it also produces a quick drop in the maximum Lorentz factor behind the shock (owing to the spreading of the initial Γ peak; see Figure 6). The Lorentz factor eventually converges to the correct BMK solution at $\Gamma \sim 10$ at

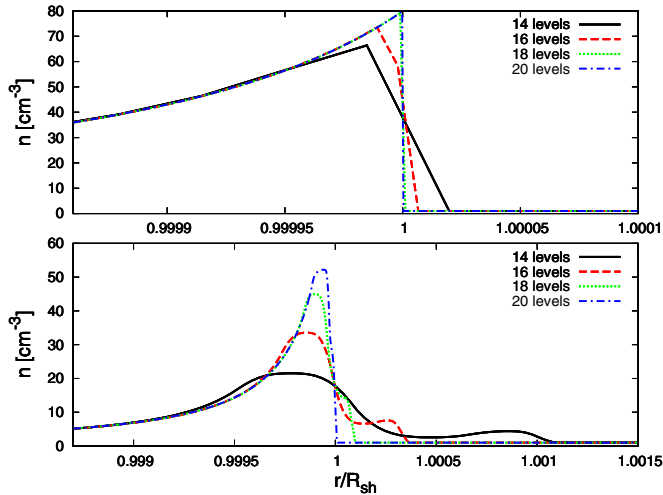


Figure 5. Number density profile (in the lab frame) for different resolutions for the case $k = 0$ at the beginning of the simulation ($t = 148$ days, upper panel) and $t = 156$ days (lower panel).

(A color version of this figure is available in the online journal.)

the largest resolution used (18 levels of refinement). Figure 6 also shows the effect of decreasing the maximum level of resolution during the evolution of the simulation (Granot et al. 2001; Zhang & MacFadyen 2009; De Colle et al. 2011). As can be appreciated from Figure 6, the decrease in the resolution produces a slower convergence to the BMK solution. The time evolution of Γ from Zhang & MacFadyen (2009) included in Figure 6 is similar to our low-resolution (14 levels) 1D simulation, corresponding approximately to the resolution achievable in multi-dimensional simulations. The noise in the Zhang & MacFadyen (2009) curve is due to a larger temporal sampling. A proper treatment of the tiny ultrarelativistic post-shock region would require a larger resolution or alternatively a much less diffusive method, such as high-order (coupled to high resolution) or Lagrangian–Eulerian methods (e.g., Kobayashi et al. 1999).

The specific numerical resolution required is determined by the relevant structure one needs to resolve. The hardest to resolve, in our case, is the initial BMK shell (Δ) at the initial time (t_0) or radius (R_0). Its effective width does not have a unique definition, but it can be parameterized as

$$\Delta_0 = a \frac{R_0}{\Gamma_{\text{sh}}^2(R_0)}, \quad (61)$$

where the numerical factor a can be evaluated using the BMK self-similar solution.⁹ Defining Δ_0 as the width of the region behind the shock that contains a fraction f of the total energy (E) or rest mass (M), respectively, results in

$$a = \frac{(1-f)^{-\alpha} - 1}{2(4-k)}, \quad \alpha_E = \frac{3(4-k)}{17-4k}, \quad \alpha_M = \frac{4-k}{3-k}. \quad (62)$$

For $f = 1/2$, this gives $a_E = 0.0789, 0.103, 0.147$ and $a_M = 0.190, 0.305, 0.750$ for $k = 0, 1, 2$, respectively.

One can then similarly express the numerical resolution in terms of a parameter a_{res} ,

$$\Delta r_{\text{min}} = a_{\text{res}} \frac{R_0}{\Gamma_{\text{sh}}^2(R_0)}, \quad (63)$$

⁹ Note that if one uses $\Gamma(R_0, \chi = 1)$ instead of $\Gamma_{\text{sh}}(R_0)$ in Equation (61), then the value of the numerical coefficient a would be smaller by a factor of two.

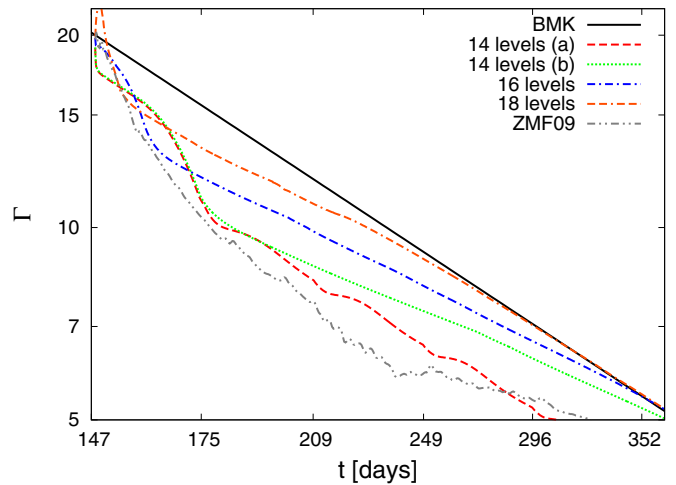


Figure 6. Maximum Lorentz factor in the post-shock region (measured in the lab frame) as a function of time. The simulations (with $k = 0$) start at $t \sim 147$ days with a Lorentz factor of 20. The curves shown correspond to the expected BMK self-similar solution; 14, 16, and 18 levels of refinement with a fixed maximum level of refinement; and results of the Zhang & MacFadyen (2009) two-dimensional simulations. For 14 levels of refinement we show two curves, either (a) with or (b) without decreasing the maximum level of refinement with time. Each label on the x -axis corresponds to the time when the maximum resolution drops by a factor of two, so that, for instance, the simulation with initially 14 levels of refinement drops to 13 levels after 175 days, 12 after 209 days, and so on.

(A color version of this figure is available in the online journal.)

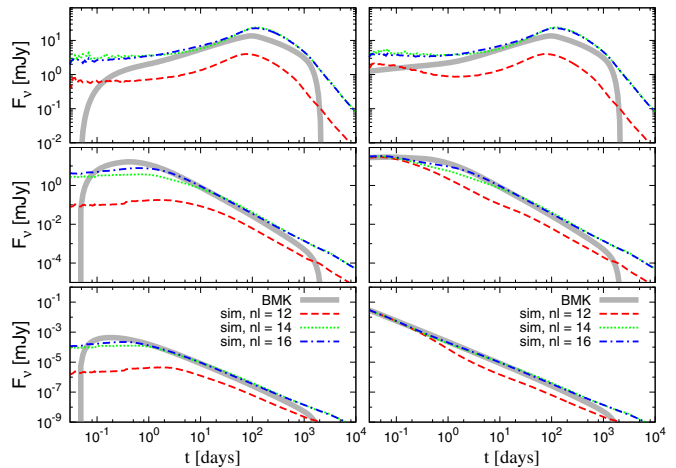


Figure 7. Light curves (at $10^9, 10^{13}$, and 10^{17} Hz from top to bottom) from simulations at different resolution, either including (right panels) or not including (left panels) the contribution from the synthetic light curve emitted from a Blandford–McKee self-similar blast wave with Lorentz factor between 200 and 20. The synthetic light curve (labeled BMK in the figure) emitted from a Lorentz factor between 1 and 20 (or between 1 and 200) is also shown in the left (right) panels of the figure.

(A color version of this figure is available in the online journal.)

where Δr_{min} is the smallest resolution element in the radial direction. Previous 2D jet numerical simulations with similar initial conditions used $k = 0$. In Granot et al. (2001) the initial resolution was rather poor, $a_{\text{res}} = 0.69$, while in Zhang & MacFadyen (2009) it was significantly improved, $a_{\text{res}} = 0.12$. Here, we use $a_{\text{res}} = 0.014$ for $k = 0$, which represents an order-of-magnitude improvement. For $k = 1$ and 2 we have $a_{\text{res}} = 0.022$ and 0.087, respectively.

Figure 7 shows that the light curve, computed by post-processing the results of the simulations with our radiation code, converges quickly except for $t_{\text{obs}} \lesssim 0.5$ days, where part of the

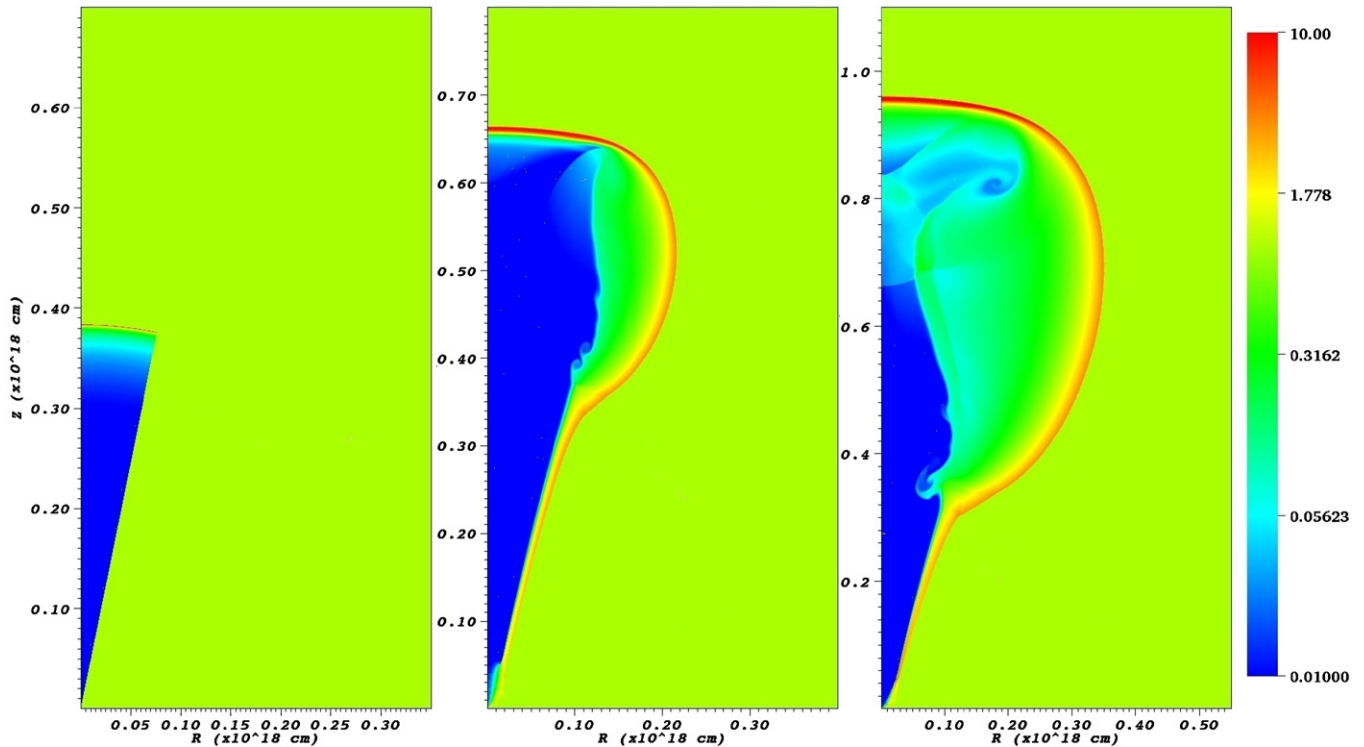


Figure 8. Lab-frame density stratification snapshots of the 2D simulation at 147 days (left), 256 days (center), and 372 days (right panel).

(A color version of this figure is available in the online journal.)

flux, which should be generated from regions with $\Gamma \sim 20$, is shifted to a lower t_{obs} . That can be in part compensated by adding the contribution coming from the jet decelerating with $20 \leq \Gamma \leq 200$, computed by mapping in the radiation code a BMK self-similar solution. As shown in Figure 7 (right), the sum of the synthetic flux with $20 \leq \Gamma \leq 200$ and the flux computed from the results of the simulation with $1 \leq \Gamma \leq 20$ produces a valley (shallower for increasing resolutions) for $t_{\text{obs}} \sim 1$ day. This artificial feature is due to relaxation from the initial conditions to the numerical solution and gradually disappears as the resolution is increased. A comparison between the light curve computed from the 1D simulation (with $k = 0$) and the semianalytical calculations from Granot & Sari (2002) is shown in Appendix A.

4.4. Two-dimensional Simulations for $k = 0$

Figure 8 shows snapshots representing the early evolutionary stages of the jet density. During the relativistic phase, there is only modest lateral expansion. As portions of the jet expand laterally, a rarefaction front moves toward the jet axis. The strong shear present at the contact discontinuity drives shearing instabilities that have, however, a negligible effect on the shock dynamics and afterglow radiation coming from the jet. At the jet break time $t = t_{\text{JB}} \sim 8.7$ yr, the lateral expansion becomes more vigorous, and at later stages (on times $\gg t_{\text{NR}}$) the jet slowly converges to a spherical shape. Although it is not possible to make a quantitative comparison, our results qualitatively resemble those of Zhang & MacFadyen (2009, see their Figure 2 for a direct comparison) as well as those of Granot et al. (2001).

While theoretical arguments (Gruzinov 2000; Wang et al. 2002) seem to indicate that the shock front should be stable to linear perturbations for either a uniform or a wind density profile of the ambient medium, recent simulations by Meliani

& Keppens (2010) observe the development of instabilities in the shock front. The development of similar instabilities is also observed by De Colle et al. (2011) relative to the case of a stratified medium with $k = 2$, while it is not observed in the simulations presented in this paper (despite using the same HLL Riemann solver as Meliani & Keppens 2010 and similar initial conditions), consistently with the results by Zhang & MacFadyen (2009). The different results in the simulation seem to imply a numerical origin for the instabilities observed by Meliani & Keppens (2010), although further investigation is needed to better understand the problem.

The afterglow light curves computed from our 2D jet simulation assume that the observer is located along the jet symmetry axis ($\theta_{\text{obs}} = 0$). To facilitate comparison with the results of Zhang & MacFadyen (2009), we choose the same parameters for the afterglow calculation: $\epsilon_B = \epsilon_e = 0.1$, $z = 1$, and $p = 2.5$, in addition to the same values for the parameters to determine the hydrodynamics ($E_{\text{iso}} = 10^{53}$ erg, $n_{\text{ext}} = 1 \text{ cm}^{-3}$, and $\theta_0 = 0.2$ rad).

As in the 1D case, the afterglow emission (Figure 9) shows a shallow valley at $t \lesssim 1$ day, owing to a lack of resolution into the region immediately behind the high-relativistic shock. Figure 9 (lower panel) shows a comparison with a 2D “wedge” (computed by using a 1D simulation mapped on a wedge with $\theta \leq 0.2$; the finite resolution of this 1D simulation is affecting the light curves at the earliest times as shown in Figure 9). Before the jet break time, the 2D light curve from the simulation is very similar to that from a 2D wedge with the same (initial) isotropic energy, indicating that little sideways expansion takes place before the jet break, in agreement with previous analytical (e.g., Rhoads 1999) and numerical (Granot et al. 2001) results. After the jet break time, however, the flux from the 2D simulation becomes lower than that for the corresponding wedge, and the difference between the two

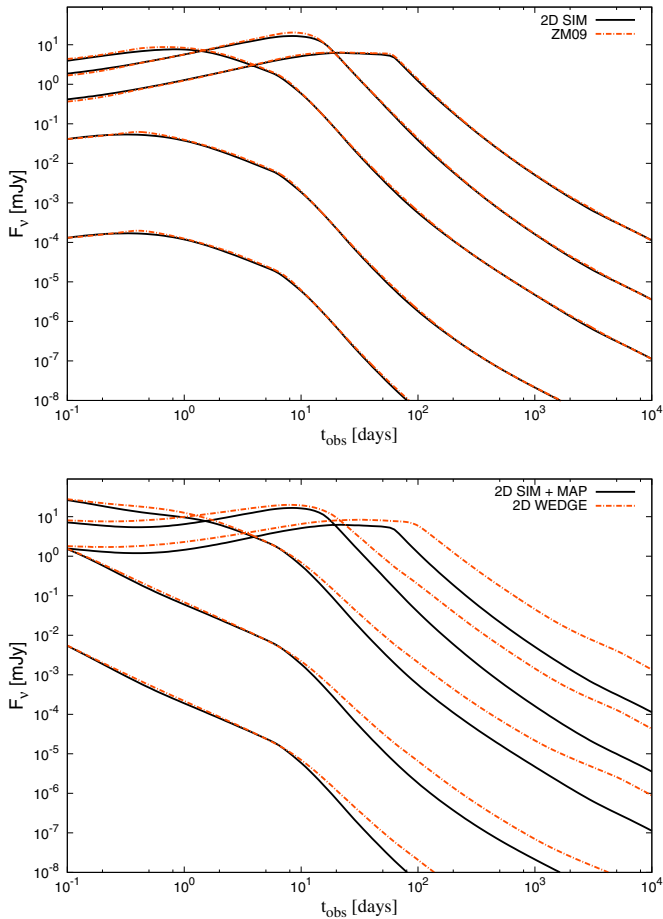


Figure 9. Afterglow emission at 10^9 , 10^{11} , 10^{13} , and 10^{15} Hz from the 2D simulation compared with a 2D wedge (lower panel) and the results from Zhang & MacFadyen (2009) (upper panel).

(A color version of this figure is available in the online journal.)

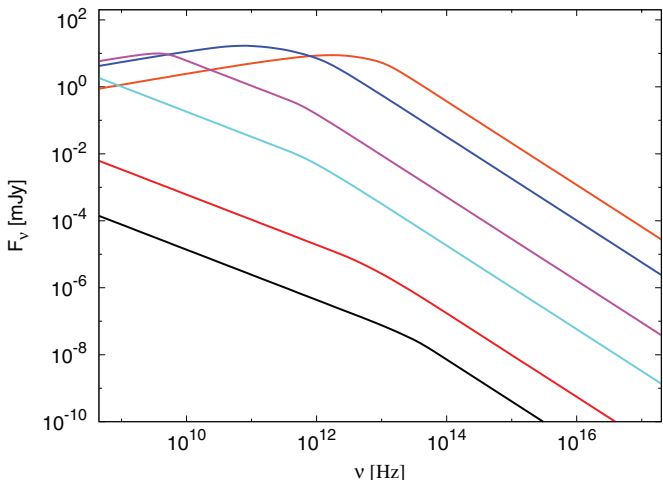


Figure 10. Spectra at $t_{\text{obs}} = 0.1, 1, 10, 100, 1000$ days (black, red, green, blue, purple).

(A color version of this figure is available in the online journal.)

gradually increases with time, as the lateral spreading of the jet gradually increases during the relativistic phase and then more rapidly during the Newtonian phase (until at very late times spherical symmetry is approached). Our calculated afterglow emission and spectra agree very well with Zhang & MacFadyen

(2009) (Figure 9, upper panel and Figure 10) in the flux both before and after the jet break.

5. CONCLUSIONS

In this paper, we have presented a detailed description of the new state-of-the-art AMR, relativistic hydrodynamics code Mezcatal-SRHD, and of the radiation code used to compute the synchrotron emission from the output of the hydrodynamics simulation. The proper implementation of the SRHD algorithm has been verified by running standard one- and multi-dimensional tests, which are presented in Appendix B. The code has been applied to the study of the propagation of ultra-relativistic impulsive blast waves in both 1D and 2D spherical coordinates.

We have studied for the first time the deceleration of relativistic impulsive blast waves in one dimension propagating in a stratified medium and find that the deceleration to non-relativistic speeds happens on scales R_{NR} from a few (for $k = 0$) to several times larger than the Sedov length L_S . Taking R_{NR} as the radius where $R_{\text{ST}}(t) = ct$ gives the expression $R_{\text{NR}}/L_S = [4\pi\alpha_k/(3-k)]^{1/(3-k)}$, which illustrates how R_{NR}/L_S increases with the degree of stratification of the ambient medium where the shock is propagating. These results have been described in detail using a simple semianalytical formula, derived from energy conservation, which gives the correct scaling of the position and velocity of the shock as a function of time.

The results obtained by the radiation code were validated by a comparison with semianalytical results and with those obtained in previous numerical works. We have also shown that while the resolution is a key factor to properly recover the correct dynamical evolution of the system (with some of the parameters not yet converging, e.g., the shock Lorentz factor), when the contribution from the radiation produced by the jet before the onset of the simulation (in our case $20 \leq \Gamma_{\text{sh}}/\sqrt{2} \leq 200$) is included in the calculation, the resulting light curve becomes much less sensitive to the exact resolution.

In an upcoming paper, we will extend the results of the simulations presented here to include multi-dimensional simulations in a stratified medium. The study of the contribution of the magnetic field on the jet dynamics and afterglow radiation is left for future works.

This research was supported by the David and Lucille Packard Foundation (E.R.R. and F.D.C.), the NSF (E.R.R.) (AST-0847563), the ERC advanced research grant ‘‘GRBs,’’ and a DGAPA postdoctoral grant from UNAM (D.L.C.). We thank Weiqun Zhang for sharing data from his 2D simulations with us (used in Figure 6).

APPENDIX A

EVALUATING THE APPROXIMATIONS USED IN THE ELECTRON COOLING FREQUENCY ESTIMATION

A comparison between the light curve computed by mapping in the radiation code a blast wave described by a BMK self-similar solution and the semianalytical calculations from Granot & Sari (2002) is shown in Figure 11. While Granot & Sari (2002) obtained smooth spectral breaks, for simplicity we use here their broken power-law prescription (without synchrotron self-absorption). In that work the afterglow emission from the BMK solution is calculated for an exact local synchrotron spectral emissivity while analytically calculating the electron energy

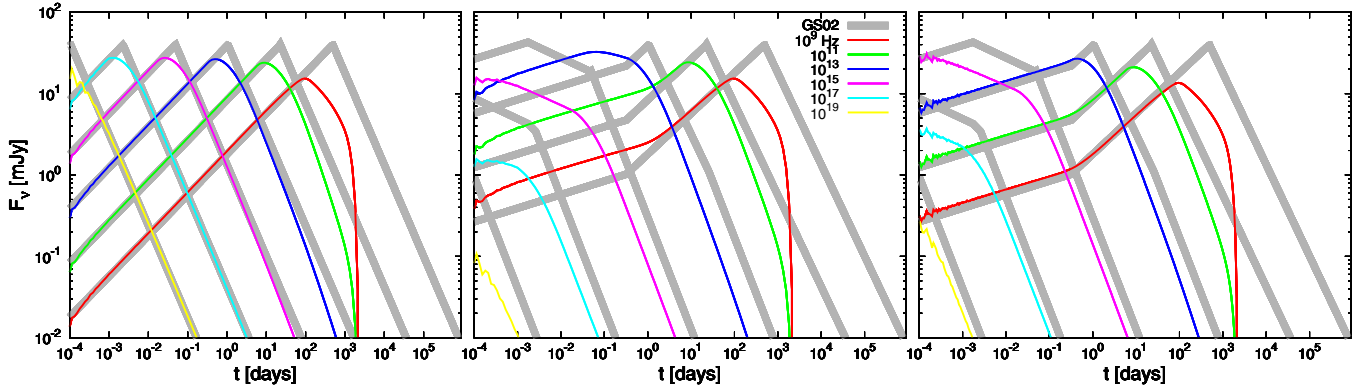


Figure 11. Comparison between light curves (at 10^9 , 10^{11} , 10^{13} , 10^{15} , and 10^{17} Hz) computed from a Blandford–McKee self-similar blast wave with Lorentz factor between 600 and 1 and the semianalytical results from Granot & Sari (2002). Left panel: simple emission model excluding electron cooling (Equation (44)). Center panel: light curve computed by using an approximated emission model for the electron cooling (Equations (39)). Right panel: Same as the center panel, but with a cooling frequency four times larger.

(A color version of this figure is available in the online journal.)

distribution everywhere by following its evolution from the shock front (where it is assumed to be a pure power law) due to radiative and adiabatic cooling. The light curve computed by using a simplified emission model (Equation (44)) that neglects electron cooling altogether is in very good agreement with the GS02 semianalytical results (see Figure 11). The light curve computed by using an approximated electron cooling presents three breaks at low frequencies (corresponding to the transitions $\nu < \nu_c < \nu_m$ with the scaling $F_\nu \propto t^{1/6} \rightarrow \nu < \nu_m < \nu_c$ with $F_\nu \propto t^{1/2} \rightarrow \nu_m < \nu < \nu_c$ with $F_\nu \propto t^{3(1-p)/4} \rightarrow \nu_m < \nu_c < \nu$ with $F_\nu \propto t^{(2-3p)/4}$) and two breaks at high frequencies (corresponding to $\nu < \nu_c < \nu_m$ with $F_\nu \propto t^{1/6} \rightarrow \nu_c < \nu < \nu_m$ with $F_\nu \propto t^{-1/4} \rightarrow \nu_c < \nu_m < \nu$ with $F_\nu \propto t^{(2-3p)/4}$). As noticed in Figure 11, our estimation of the cooling break frequency ν_c assuming that the electrons cool at their current local cooling rate over the dynamical time (see Equations (39)) underestimates the cooling frequency determined by GS02. For instance, an increase in ν_c of a factor of four produces a better agreement with the GS02 results (Figure 11, right panel). It is worthwhile to stress that, while the mapped BMK light curve and the GS02 results are applicable only for (highly) relativistic flows, the light curve computed from the numerical simulations is valid during the entire deceleration of the flow to nonrelativistic speeds. Finally, we note that at $\nu \lesssim 10^9$ Hz, self-absorption dominates and the light curves computed with our simple prescription are inaccurate.

APPENDIX B

NUMERICAL TESTS

We present in this section a series of 1D shock tubes and multi-dimensional tests.

B.1. One-dimensional Shock Tubes

Shock tube tests are used as standard tests as they are simple to implement and the exact analytical solution is known. The tests were performed using a grid with size $0 \leq x \leq 1$, with an initial discontinuity at $x = 0.5$. Here and in the following, we refer to the left/right-hand side of the discontinuity with the suffixes L/R . In all the tests, we use a grid with 50 cells at the lowest level, with four levels of refinement, corresponding to an effective resolution of 400 cells. We also make high-resolution runs of the same tests, employing 400 cells at the lowest level, with four levels of refinement, corresponding to an effective

resolution of 3200 cells. The Courant number is fixed equal to 0.8 in all tests, with a final integration time of $t = 0.4$. The polytropic index is fixed equal to $4/3$ in the first shock tube test and $5/3$ in all other tests. As described in the following, in all the tests the exact solution is properly recovered.

The first test consists of a low-relativistic flow with a left state given by $p_L = 1$, $\rho_L = 1$, and $v_L = 0.9$, corresponding to a Lorentz factor of $\Gamma \approx 2.3$, and a right state given by $p_R = 10$, $\rho_R = 1$, and $v_R = 0$. The evolution of this shock tube consists of two shocks and a stationary contact discontinuity. Small oscillations, similar to those observed by previous authors (e.g., Lucas-Serrano et al. 2004; Wang et al. 2008), are present in the post-shock region.

The second shock tube consists of a low-relativistic flow with a left state given by $p_L = 10$, $\rho_L = 1$, and $v_L = -0.6$ and a right state given by $p_R = 20$, $\rho_R = 10$, and $v_R = 0.5$. In this test, two rarefaction waves are produced, together with a left moving contact discontinuity. Both rarefaction waves are properly recovered, while the contact discontinuity is smeared over ~ 10 cells.

The last two tests are taken from Donat (1998) and refer to blast wave explosions. The third shock tube consists of a left state given by $p_L = 40/3$, $\rho_L = 10$, and a right state given by $p_R = 10^{-6}$, $\rho_R = 1$, while in the last test the left state is given by $p_L = 1000$, $\rho_L = 1$, and the right state is given by $p_R = 0.01$, $\rho_R = 1$. The large pressure gradient produces a mildly relativistic shock (test 3) and a highly relativistic shock (test 4) with $\Gamma \approx 6$. As can be seen in Figure 12, in both cases the solution consists of a strong shock moving to the right and a rarefaction wave moving to the left. No oscillations are present in the solution. The shock is resolved within ~ 4 cells, while the contact discontinuity is smeared over several cells. That is expected, owing to the intrinsic diffusive properties of the HLL schemes. In the second blast wave problem, the size of the thin dense shell in the post-shock region consists of only ≈ 4 cells with the resolution employed. As a consequence, the exact value of the density is not recovered at low resolution. However, this region is properly resolved in the high-resolution run.

B.2. Multi-dimensional Tests

B.2.1. Relativistic 2D Riemann Problem

This test has been studied in the nonrelativistic case by Lax & Liu (1998) and extended to the SRHD case by Del Zanna &

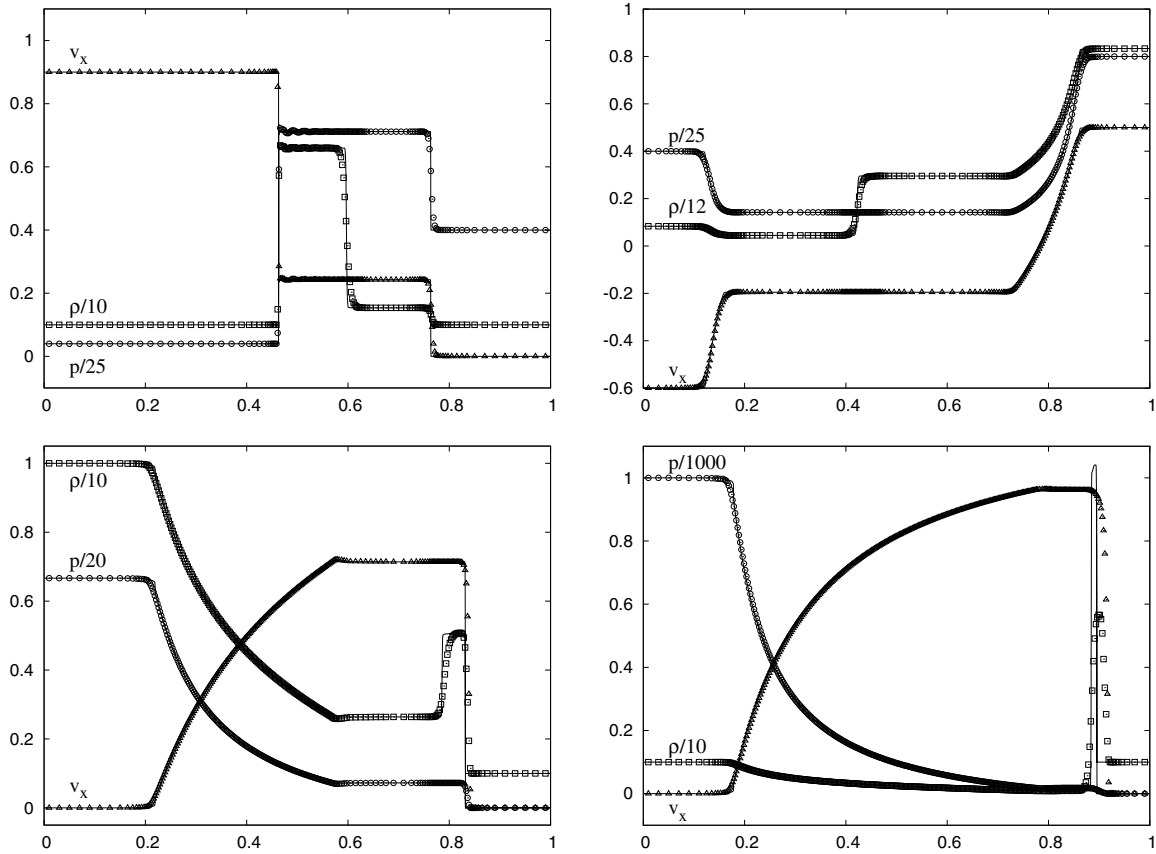


Figure 12. One-dimensional shock tube problems at $t = 0.4$. The variables shown are density, velocity, and pressure. The initial discontinuity was set at $x = 0.5$; the Courant number is equal to 0.8, with a maximum resolution of 400 cells (points) and 3200 cells (lines). The panels correspond to first (upper left), second (upper right), third (lower left), and fourth (lower right) shock tube tests (see the text for a detailed description of the initial conditions).

Bucciantini (2002). It has been widely used recently as a test for multi-dimensional SRHD codes (e.g., Lucas-Serrano et al. 2004; Wang et al. 2008). The computational domain (at $t = 0$) is divided into four regions:

$$\begin{aligned}
 (\rho, v_x, v_y, p)^{\text{NE}} &= (0.1, 0, 0, 0.01) & \text{if } x \geq 0.5, y \geq 0.5 \\
 (\rho, v_x, v_y, p)^{\text{NW}} &= (0.1, 0.99, 0, 1) & \text{if } x \leq 0.5, y \geq 0.5 \\
 (\rho, v_x, v_y, p)^{\text{SW}} &= (0.5, 0, 0, 1) & \text{if } x \geq 0.5, y \leq 0.5 \\
 (\rho, v_x, v_y, p)^{\text{SE}} &= (0.1, 0, 0.99, 1) & \text{if } x \leq 0.5, y \leq 0.5.
 \end{aligned}$$

We use a uniform grid with 400×400 cells, an adiabatic EOS with constant $\gamma = 5/3$, and outflow boundary conditions. The simulations end at $t = 4$. To better resolve the contact discontinuity, a more compressive monotized central difference limiter is used here. The results are shown in Figure 13. The initial discontinuities across the four regions of the grid produce a stationary contact discontinuity (with jumps in transverse velocities) between SW–NW and SE–SW and shocks between NE–NW and SE–SW. These shocks produce an elongated jet-like structure on the diagonal. These features, together with the curved shock in the SW region, are qualitatively similar to those obtained by previous authors.

B.2.2. Emery Step

The ‘‘Emery step’’ test has become a standard test for both nonrelativistic and relativistic hydrodynamic codes, and it consists of a wind moving through a tunnel. Our initial conditions closely follow those by Lucas-Serrano et al. (2004).

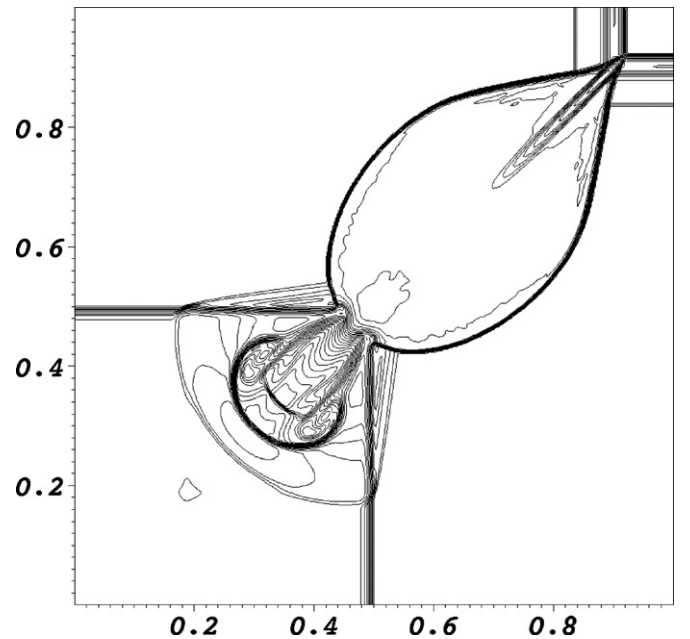


Figure 13. Logarithm of the density for the relativistic 2D Riemann problem at $t = 0.4$. Thirty equally spaced contours are plotted in the figure.

A relativistic flow moves initially horizontally with velocity $v_x = 0.999c$, corresponding to a Lorentz factor of $\Gamma \approx 7$. The density is initially fixed at $\rho = 1.4$ everywhere, with a pressure of $p = 1/9$ and an adiabatic index of $\gamma = 7/4$, corresponding

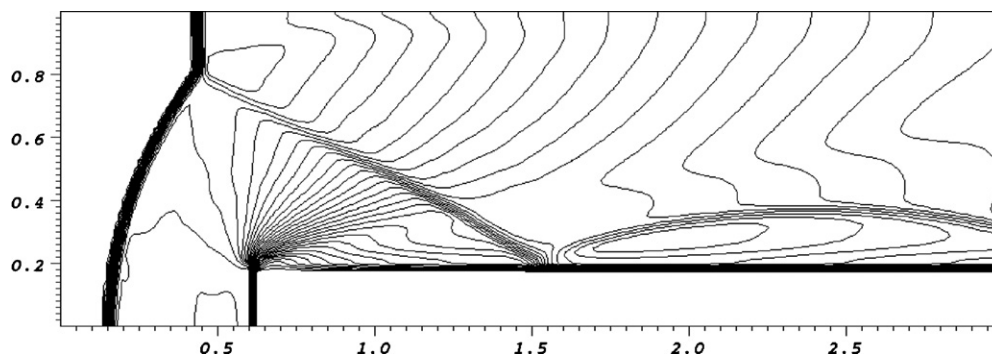


Figure 14. Logarithm of the density for the Emery step problem at $t = 4.26$. Thirty equally spaced contours are plotted in the figure.

to a Newtonian Mach number of $M = 3$. The size of the tunnel is $0 \leq x \leq 3$ and $0 \leq y \leq 1$. A step is located in the region defined by $x \geq 0.6$, $y \leq 0.2$. Inflow boundary conditions (with the same values used to fill the tunnel initially) are fixed at the left boundary. Outflow boundary conditions are fixed at the right boundary, while reflecting boundary conditions are fixed at the upper, lower, and step boundaries. We use a uniform grid with 240×80 cells, with the HLL method coupled to the MC limiter.

Figure 14 shows the density stratification at $t = 4.26$. As the relativistic flow collides with the step, a reverse shock is formed. This shock front is reflected from the upper boundary forming a stationary Mach stem. The results of this test are similar to those of Lucas-Serrano et al. (2004).

REFERENCES

- Abdo, A. A., Ackermann, M., Ajello, M., et al. 2009a, *ApJ*, 706, L138
- Abdo, A. A., Ackermann, M., Arimoto, M., et al. 2009b, *Science*, 323, 1688
- Ackermann, M., Asano, K., Atwood, W. B., et al. 2010, *ApJ*, 716, 1178
- Anile, A. M. 1989, *Relativistic Fluids and Magneto-fluids: With Applications in Astrophysics and Plasma Physics* (Cambridge: Cambridge Univ. Press)
- Anninos, P., Fragile, P. C., & Salmonson, J. D. 2005, *ApJ*, 635, 723
- Barkov, M. V., & Baushev, A. N. 2011, *New Astron.*, 16, 46
- Barkov, M. V., & Komissarov, S. S. 2008, *MNRAS*, 385, L28
- Beloborodov, A. M., & Uhm, Z. L. 2006, *ApJ*, 651, L1
- Berger, M. J., & Olinger, J. 1984, *J. Comput. Phys.*, 53, 484
- Blandford, R. D., & McKee, C. F. 1976, *PhFI*, 19, 1130
- Blandford, R. D., & Payne, D. G. 1982, *MNRAS*, 199, 883
- Blandford, R. D., & Znajek, R. L. 1977, *MNRAS*, 179, 433
- Bucciantini, N., Quataert, E., Arons, J., Metzger, B. D., & Thompson, T. A. 2007, *MNRAS*, 380, 1541
- Bucciantini, N., Quataert, E., Arons, J., Metzger, B. D., & Thompson, T. A. 2008, *MNRAS*, 383, L25
- Bucciantini, N., Quataert, E., Metzger, B. D., et al. 2009, *MNRAS*, 396, 2038
- Cannizzo, J. K., Gehrels, N., & Vishniac, E. T. 2004, *ApJ*, 601, 380
- Chen, W.-X., & Beloborodov, A. M. 2007, *ApJ*, 657, 383
- Chevalier, R. A., & Li, Z.-Y. 2000, *ApJ*, 536, 195
- Chiosi, C., & Maeder, A. 1986, *ARA&A*, 24, 329
- De Colle, F., & Raga, A. C. 2005, *MNRAS*, 359, 164
- De Colle, F., & Raga, A. C. 2006, *A&A*, 449, 1061
- De Colle, F., Raga, A. C., & Esquivel, A. 2008, *ApJ*, 689, 302
- De Colle, F., Ramirez-Ruiz, E., Granot, J., & Lopez-Camara, D. 2011, arXiv:1111.6667
- Del Zanna, L., & Bucciantini, N. 2002, *A&A*, 390, 1177
- Donat, R. 1998, *J. Comput. Phys.*, 146, 58
- Dursi, L. J., & Zingale, M. 2003, arXiv:astro-ph/0310891
- Eichler, D., Livio, M., Piran, T., & Schramm, D. N. 1989, *Nature*, 340, 126
- Faber, J. A., Baumgarte, T. W., Shapiro, S. L., & Taniguchi, K. 2006, *ApJ*, 641, L93
- Falle, S. A. E. G. 1991, *MNRAS*, 250, 581
- Falle, S. A. E. G., & Komissarov, S. S. 1996, *MNRAS*, 278, 586
- Fryer, D. A., Kulkarni, S. R., Sari, R., et al. 2001, *ApJ*, 562, L55
- Fryer, C. L., & Woosley, S. E. 1998, *ApJ*, 502, L9
- Gehrels, N., Ramirez-Ruiz, E., & Fox, D. B. 2009, *ARA&A*, 47, 567
- Goodman, J., & MacFadyen, A. 2008, *J. Fluid Mech.*, 604, 325
- Granot, J. 2007, *RevMexAA Conf. Ser.*, 27, 140
- Granot, J., Cohen-Tanugi, J., & do Couto e Silva, E. 2008, *ApJ*, 677, 92
- Granot, J., Komissarov, S. S., & Spitkovsky, A. 2011, *MNRAS*, 411, 1323
- Granot, J., & Königl, A. 2003, *ApJ*, 594, L83
- Granot, J., Miller, M., Piran, T., Suen, W. M., & Hughes, P. A. 2001, in *GRBs in the Afterglow Era*, ed. E. Costa, F. Frontera, & J. Hjorth (Berlin: Springer), 312
- Granot, J., Panaitescu, A., Kumar, P., & Woosley, S. E. 2002, *ApJ*, 570, L61
- Granot, J., Piran, T., & Sari, R. 1999a, *ApJ*, 527, 236
- Granot, J., Piran, T., & Sari, R. 1999b, *ApJ*, 513, 679
- Granot, J., & Ramirez-Ruiz, E. 2010, arXiv:1012.5101
- Granot, J., & Sari, R. 2002, *ApJ*, 568, 820
- Gruzinov, A. 2000, arXiv:astro-ph/0012364
- Harten, A., Lax, P., & van Leer, B. 1983, *SIAM Rev.*, 25, 35
- Hawley, J. F., & Krolik, J. H. 2006, *ApJ*, 641, 103
- Hjorth, J., Sollerman, J., Møller, P., et al. 2003, *Nature*, 423, 847
- Hughes, P. A., Miller, M. A., & Duncan, G. C. 2002, *ApJ*, 572, 713
- Inoue, T., Asano, K., & Ioka, K. 2011, *ApJ*, 734, 77
- Khokhlov, A. 1998, *J. Comput. Phys.*, 143, 519
- Kobayashi, S., Piran, T., & Sari, R. 1999, *ApJ*, 513, 669
- Komissarov, S. S., & Barkov, M. V. 2007, *MNRAS*, 382, 1029
- Kouveliotou, C., Meegan, C. A., Fishman, G. J., et al. 1993, *ApJ*, 413, L101
- Krolik, J. H., & Hawley, J. F. 2010, *The Jet Paradigm* (Lecture Notes in Physics, Vol. 794; Berlin: Springer), 265
- Kumar, P., & Granot, J. 2003, *ApJ*, 591, 1075
- Lax, P. D., & Liu, X.-D. 1998, *SIAM J. Sci. Comput.*, 19, 319
- Lee, W. H., & Ramirez-Ruiz, E. 2002, *ApJ*, 577, 893
- Lee, W. H., & Ramirez-Ruiz, E. 2006, *ApJ*, 641, 961
- Lee, W. H., & Ramirez-Ruiz, E. 2007, *New J. Phys.*, 9, 17
- Lee, W. H., Ramirez-Ruiz, E., & Page, D. 2004, *ApJ*, 608, L5
- Li, S., & Li, H. 2003, Los Alamos Report LA-UR-03-8925
- Lithwick, Y., & Sari, R. 2001, *ApJ*, 555, 540
- Lucas-Serrano, A., Font, J. A., Ibáñez, J. M., & Martí, J. M. 2004, *A&A*, 428, 703
- Lynden-Bell, D. 2003, *MNRAS*, 341, 1360
- MacFadyen, A. I., & Woosley, S. E. 1999, *ApJ*, 524, 262
- Mathews, W. G. 1971, *ApJ*, 165, 147
- McKinney, J. C. 2006, *MNRAS*, 368, 1561
- Meier, D. L. 2003, *New Astron. Rev.*, 47, 667
- Meliani, Z., & Keppens, R. 2010, *A&A*, 520, L3
- Meliani, Z., Keppens, R., Casse, F., & Giannios, D. 2007, *MNRAS*, 376, 1189
- Meszáros, P., & Rees, M. J. 1997, *ApJ*, 476, 232
- Mignone, A., & Bodo, G. 2005, *MNRAS*, 364, 126
- Mignone, A., & McKinney, J. C. 2007, *MNRAS*, 378, 1118
- Mimica, P., & Giannios, D. 2011, *MNRAS*, 418, 583
- Mimica, P., Giannios, D., & Aloy, M. A. 2009, *A&A*, 494, 879
- Mimica, P., Giannios, D., & Aloy, M. A. 2010, *MNRAS*, 407, 2501
- Mizuno, Y., Pohl, M., Niemiec, J., et al. 2011, *ApJ*, 726, 62
- Mizuno, Y., Yamada, S., Koide, S., & Shibata, K. 2004a, *ApJ*, 606, 395
- Mizuno, Y., Yamada, S., Koide, S., & Shibata, K. 2004b, *ApJ*, 615, 389
- Morsony, B. J., Lazzati, D., & Begelman, M. C. 2007, *ApJ*, 665, 569
- Nagataki, S. 2009, *ApJ*, 704, 937
- Nagataki, S., Takahashi, R., Mizuta, A., & Takiwaki, T. 2007, *ApJ*, 659, 512
- Nakar, E. 2007, *Phys. Rep.*, 442, 166
- Nakar, E., & Granot, J. 2007, *MNRAS*, 380, 1744
- Narayan, R., Paczynski, B., & Piran, T. 1992, *ApJ*, 395, L83
- Noble, S. C., Gammie, C. F., McKinney, J. C., & Del Zanna, L. 2006, *ApJ*, 641, 626
- Oechslin, R., & Janka, H.-T. 2006, *MNRAS*, 368, 1489

- Paczynski, B. 1986, *ApJ*, **308**, L43
- Panaitescu, A., & Kumar, P. 2000, *ApJ*, **543**, 66
- Petruk, O. 2000, *A&A*, **357**, 686
- Pihlström, Y. M., Taylor, G. B., Granot, J., & Doeleman, S. 2007, *ApJ*, **664**, 411
- Piran, T. 2005a, *Rev. Mod. Phys.*, **76**, 1143
- Piran, T. 2005b, *Nuovo Cimento C*, **28**, 373
- Popham, R., Woosley, S. E., & Fryer, C. 1999, *ApJ*, **518**, 356
- Proga, D., MacFadyen, A. I., Armitage, P. J., & Begelman, M. C. 2003, *ApJ*, **599**, L5
- Ramirez-Ruiz, E., Celotti, A., & Rees, M. J. 2002, *MNRAS*, **337**, 1349
- Ramirez-Ruiz, E., Dray, L. M., Madau, P., & Tout, C. A. 2001, *MNRAS*, **327**, 829
- Ramirez-Ruiz, E., García-Segura, G., Salmonson, J. D., & Pérez-Rendón, B. 2005, *ApJ*, **631**, 435
- Ramirez-Ruiz, E., & MacFadyen, A. I. 2010, *ApJ*, **716**, 1028
- Rees, M. J., & Meszaros, P. 1992, *MNRAS*, **258**, 41
- Rezzolla, L., Baiotti, L., Giacomazzo, B., Link, D., & Font, J. A. 2010, *CQGra*, **27**, 114105
- Rezzolla, L., Giacomazzo, B., Baiotti, L., et al. 2011, *ApJ*, **732**, L6
- Rhoads, J. E. 1997, *ApJ*, **487**, L1
- Rhoads, J. E. 1999, *ApJ*, **525**, 737
- Rosswog, S. 2005, *ApJ*, **634**, 1202
- Rosswog, S., & Ramirez-Ruiz, E. 2002, *MNRAS*, **336**, L7
- Rosswog, S., Ramirez-Ruiz, E., & Davies, M. B. 2003, *MNRAS*, **345**, 1077
- Rybicki, G. B., & Lightman, A. P. 1979, *Radiative Processes in Astrophysics* (New York: Wiley), 145
- Ryu, D., Chattopadhyay, I., & Choi, E. 2006, *ApJS*, **166**, 410
- Sagan, H. 1994, *Space-Filling Curves* (New York: Springer)
- Salmonson, J. D., Fragile, P. C., & Anninos, P. 2006, *ApJ*, **652**, 1508
- Sari, R., Piran, T., & Halpern, J. 1999, *ApJ*, **519**, L17
- Schneider, V., Katscher, U., Rischke, D. H., et al. 1993, *J. Comput. Phys.*, **105**, 92
- Sedov, L. I. 1959, *Similarity and Dimensional Methods in Mechanics* (New York: Academic Press)
- Stanek, K. Z., Matheson, T., Garnavich, P. M., et al. 2003, *ApJ*, **591**, L17
- Synge, J. L. (ed.) 1971, *Talking about Relativity* (Amsterdam, Netherlands: North-Holland Publishing Company), 193
- Taub, A. H. 1948, *Phys. Rev.*, **74**, 328
- Taylor, G. 1950, *Proc. R. Soc. A*, **201**, 159
- Taylor, G. B., Frail, D. A., Berger, E., & Kulkarni, S. R. 2004, *ApJ*, **609**, L1
- Taylor, G. B., Momjian, E., Pihlström, Y., Ghosh, T., & Salter, C. 2005, *ApJ*, **622**, 986
- Tchekhovskoy, A., McKinney, J. C., & Narayan, R. 2008, *MNRAS*, **388**, 551
- Toro, E. F. 2008, *Jets from Young Stars III* (Lecture Notes in Physics, Vol. 754; Berlin: Springer), 3
- Usov, V. V. 1992, *Nature*, **357**, 472
- Uzdensky, D. A., & MacFadyen, A. I. 2006, *ApJ*, **647**, 1192
- van Eerten, H. J., Leventis, K., Meliani, Z., Wijers, R. A. M. J., & Keppens, R. 2010, *MNRAS*, **403**, 300
- van Eerten, H. J., & MacFadyen, A. I. 2011, arXiv:1105.2485
- van Eerten, H. J., Meliani, Z., Wijers, R. A. M. J., & Keppens, R. 2011, *MNRAS*, **410**, 2016
- van Leer, B. 1979, *J. Comput. Phys.*, **32**, 101
- Wang, P., Abel, T., & Zhang, W. 2008, *ApJS*, **176**, 467
- Wang, X., Loeb, A., & Waxman, E. 2002, *ApJ*, **568**, 830
- Woosley, S. E. 1993, *ApJ*, **405**, 273
- Woosley, S. E., & Bloom, J. S. 2006, *ARA&A*, **44**, 507
- Wygoda, N., Waxman, E., & Frail, D. 2011, *ApJ*, **738**, L23
- Zhang, W., & MacFadyen, A. I. 2009, *ApJ*, **698**, 1261
- Zhang, W., MacFadyen, A., & Wang, P. 2009, *ApJ*, **692**, L40
- Zhang, W., Woosley, S. E., & MacFadyen, A. I. 2003, *ApJ*, **586**, 356